Chinese Journal of Chemical Engineering 60 (2023) 275–292

Contents lists available at ScienceDirect

Chinese Journal of Chemical Engineering

journal homepage: www.elsevier.com/locate/CJChE

Full Length Article

Mechanisms and reusability potentials of zirconium-polyaziridine-engineered tiger nut residue towards anionic pollutants

Alexander Nti Kani, Evans Dovi, Aaron Albert Aryee, Runping Han *, Zhaohui Li, Lingbo Qu

College of Chemistry, Green Catalysis Center, Zhengzhou University, Zhengzhou 450001, China

ARTICLE INFO

Article history:
Received 2 October 2022
Received in revised form 19 January 2023
Accepted 7 February 2023
Available online 14 February 2023

Keywords:
Adsorption
Modified tiger nut residue
Alizarin red
Phosphate
Leaching
Regeneration

ABSTRACT

Access to fresh water, its availability, and its quality are a global challenge to humanity, largely due to human activities in the environment. Thus, global water security has been jeopardized, requiring urgent remediation to safeguard our very existence. Hence, a novel and facilely engineered zirconium and polyethylenimine adsorbent based on tiger nut residue (TNR) was prepared, and its adsorptive capabilities towards a model dyestuff and nutrient were invested through a batch adsorption method. The developed adsorbent, zirconium-polyethylenimine-engineered tiger nut residue (TNR@PEI–Zr) was characterised by scanning electron microscopy, Fourier-transform infrared spectroscopy, X-ray diffraction analysis, and X-ray photoelectron spectroscopy to understand its morphology and surface chemistry and predict its adsorption mechanism. TNR@PEI–Zr had a pH point of zero charge (pH_{zpc}) of 6.7. The introduction of salts inhibited the removal efficiency of Alizarin red (AR) and phosphate (PO_4^{3-}) in the order of HCO_3^- > SO_4^{2-} > Cl^-. Increasing temperatures (293–313 K) favoured the adsorption process at pH 3. The Langmuir model suited the adsorption processes of both AR and PO_4^{3-}, implying homogenous and monolayer removal of pollutants with a maximal capacity of 537.8 mg·g^{-1} and 100.5 mg·g^{-1} at a dose of 0.01 g, respectively. The rate-determining steps of AR and PO_4^{3-} followed a pseudo-second-order kinetic model and were thermodynamically spontaneous with an increase in randomness at the solid-solution interface. The adsorbent's recyclability was notable and outperformed most adsorbents in terms of removal efficiency. TNR@PEI–Zr was found to be stable, and its use in practical wastewater decontamination was effective, ecologically acceptable and free of secondary pollution problems.

1. Introduction

The most pressing worry in recent years has been poor water quality and its shortage globally. The prevalence of dye pollutants resulting from the ever-growing dyeing industry, which consumes the highest amount of fresh water and is responsible for the huge amounts of dye stuff running into our water bodies, has prompted widespread environmental and economic concerns, owing to restricted water supplies and human need for fresh water [1]. The discharged wastewater containing synthetic dyes has jeopardized global water security and, if not properly treated, may pose major health risks to humans, including respiratory ailments, cancer, and other issues [2,3].

Alizarin red S (1,2-dihydroxy-9,10-anthraquinonesulfonic acid sodium salt) (AR), an anthraquinone dye that is water soluble, has been extensively employed in textile industries since antiquity, and its emission disrupts the environment and offers a direct hazard to humans and animals [4]. It possesses a high level of physiochemical, optical, and thermal stability, making deterioration difficult. As a result, treating wastewater containing such a dye is critical [5]. To safeguard the environment, an appropriate and cost-effective method for removing them from wastewaters should be designed.

Water management must accomplish advanced phosphorus (P) treatment to decrease water eutrophication and meet more stringent wastewater discharge rules by reducing the concentration of phosphorus present as phosphate (PO_4^{3-}), a key macronutrient element required for the growth of organisms, before discharge into the environment. This is because phosphate at concentrations above 0.02 mg·L^{-1} is reported to result in algal bloom and thus 0.1 mg·L^{-1} is the baseline allowable limit for portable water as set by the World Health Organization [6,7].

Public health concerns have resulted in some strict regulations which require these noxious contaminants to be removed to acceptable levels before discharge into water bodies.

* Corresponding author.
E-mail address: rphan67@zzu.edu.cn (R. Han).

https://doi.org/10.1016/j.cjche.2023.02.003
1004-9541/

Adsorption has been explored as one of the most efficient techniques in pollutant removal from wastewater by employing efficient materials as adsorbents. The ease of design and operation, low cost and its stability without requiring high profile technical skills promotes the adsorption process as the most reliable and facile process to use in pollutant decontamination [7,8].

Metal-modified materials are well known for their ability to enhance the selective removal of negatively charged contaminants in wastewater [9,10]. This explains why zirconium (Zr) oxides/hydroxides have a high adsorption affinity for a variety of compounds. Because of its porous and highly hydrated structure, amorphous ZrO_2 has a high adsorption capacity, allowing contaminants to permeate within the structure rather than being limited to the exterior surface site as well as forming stable complexes with its empty orbitals to bind anionic pollutants. This is attributed to the facile loading of Zr(IV) on some suitable functional groups such as the carboxyl groups, hydroxyl groups and amino groups on functional materials as well as the formation of microporous system within the interlayer space which improves the specific area, pore volume, and basal spacing [11–13].

Several researches have documented the creation of Zr-modified adsorbents and its composites and explored their adsorption potentials over wide variety pollutants in waste water. Such Zr-modified materials includes zirconium modified iminodiacetic acid magnetic peanut husk, zirconium-loaded orange waste gel, Zr-pillared montmorillonite, zirconium-loaded activated carbon adsorbent, zirconium-modified activated sludge, and magnetic zirconium–iron oxide nanoparticles [11,12,14].

Therefore, in principle, zirconium-engineered tiger nut residue (TNR) might be able to enhance the adsorption of Alizarin red and phosphate. Meanwhile, only limited studies have focused on the development of Zr-modified agricultural waste materials for such pollutant adsorption. In addition, polyethylenimine (PEI) grafted materials have been reported as showing good adsorptive capacities and possess advantageous characteristics in terms of cost, chemical stability and environmental friendliness as observed in my earlier works where PEI modified tiger nut residue was used to efficiently remove Congo red. In order to inherit the advantages of these two kinds of adsorbents, a novel adsorbent containing zirconium and PEI was engineered through an environmentally friendly process, and its potential removal efficiency towards a dyestuff pollutant and nutrient was explored and reported for the first time.

There is no comprehensive report on the adsorptive potentials of zirconium–PEI-engineered TNR towards anionic pollutants, as far as the authors are aware. We, therefore, engineered TNR with zirconium and PEI to take full advantage of their properties to enhance the adsorptive capacity of TNR and realise its full potential as an agricultural waste material in pollutant decontamination. Also, the developed adsorbent compares well with other reported adsorbents towards the removal of PO_4^{3-} and outperforms most adsorbents in the removal of AR.

The goals of this study were to: (1) synthesise Zr(IV) engineered tiger nut residue as a new functional adsorbent; (2) characterise the obtained adsorbent using various experimental techniques such as scanning electron microscopy (SEM), Brunauer–Emmett–Teller (BET) analysis, Fourier-transform infrared spectroscopy (FTIR), X-ray diffraction analysis (XRD) and X-ray photoelectron spectroscopy (XPS); (3) use a batch procedure to assess the adsorption performance of TNR@PEI–Zr towards a model dye (AR) and nutrient (PO_4^{3-}); (4) investigate the adsorption isotherms, kinetics, thermodynamics, and influence of competing ions on AR removal; (5) conduct desorption and regeneration/reusability investigations as well as leaching test to assess the stability, potential applicability of the designed adsorbent in waste water; and (6) investigate the underlying mechanism of AR and PO_4^{3-} adsorption onto TNR@PEI–Zr.

2. Methodology

2.1. Chemicals and reagents

Polyethyleneimine (≥99%, PEI), glutaraldehyde (≥25%, GA), zirconium oxychloride octahydrate (99%, $ZrOCl_2{\cdot}8H_2O$), Alizarin red (99%, AR), and potassium hydrogen phosphate (≥99%, KH_2PO_4) were acquired from Aladdin Reagent Co. ltd., Shanghai, China. Sodium bicarbonate (≥99.8%, $NaHCO_3$), sodium sulphate (≥99%, Na_2SO_4), hydrochloric acid (37%, HCl), sodium hydroxide (≥99%, NaOH), and sodium chloride (≥99.5%, NaCl) were purchased from Zhengzhou Chemical Corporation, Zhengzhou, China. All chemicals used were of analytical graded and as such were used without further purification.

2.2. Preparation of zirconium and polyaziridine engineered tiger nut residue adsorbent material (TNR@PEI–Zr)

The zirconium and polyethyleneimine engineered tiger nut residue (TNR@PEI–Zr) was prepared by loading zirconium onto TNR@PEI. TNR@PEI was prepared by a simple facile cross-linking method as described elsewhere by Kani *et al.* [15]. Briefly, about 2 g of TNR was dispensed into a conical flask containing 100 ml of 30% PEI and swirled at room temperature for 12 h. Thereafter, 10 ml of 5% GA was added and mixed at room temperature for another 2 h. The resulting material (TNR@PEI) was washed several times with distilled water and oven dried at 333 K. Then about, 1 g of the prepared TNR-PEI was added into a 100 ml solution of 0.05 $mol{\cdot}L^{-1}$ $ZrOCl_2{\cdot}8H_2O$ with an adjusted pH of 9 in an Erlenmeyer flask. The flask was agitated for 12 h in a thermostat shaker at 303 K. Thereafter, the zirconium engineered adsorbent (TNR@PEI–Zr) was separated and then washed with distilled water to a neutral pH and then placed in an oven at 333 K. During the oven drying process, the engineered adsorbent was gently stirred every 2 h to reduce the possibility of agglomerations. Thus, the obtained biomass was kept in an airtight container and labelled (TNR@PEI–Zr). The biosorbent developed (TNR@PEI–Zr) was stored in an airtight container.

2.3. List of equipment

The equipment used to examine and study the morphology of the adsorbent, quantify the concentrations of adsorbate, and predict the underlying mechanism of adsorption is presented below. The thermostatic oscillator (KW-1000DB, Kexi Instrument, China) was used for the batch adsorption, while the visible spectrophotometry (UV–Vis, TU-1900, Persee, China) was used to measure the residual concentration of the pollutants. The Brunauer–Emmett–Teller method (BET, ASAP2420-4MP, Micromeritics, USA) was used to determine the surface region, total pore volume, and average pore diameter of the adsorbent materials. Fourier transform infrared spectroscopy (FTIR, Nicolet iS50, Thermo Fisher Scientific, USA) was used to study the functional groups present on the adsorbent surface. The scanning electron microscopy (SEM, Su8020, Hitachi, Japan) was employed to verify the surface structure of TNR@PEI–Zr. With the help of X-ray diffraction spectroscopy (XRD, X'Pert PRO MPD, PANalytical, Netherlands), the crystal structure of the absorbents was examined. X-ray photoelectron spectroscopy (XPS, Escalab 250Xi, Thermo Fisher Scientific) was employed to characterize the surface chemistry of engineered adsorbents and to elucidate the adsorption mechanisms. The pH

point of zero charge (pH_{zpc}) values of TNR@PEI–Zr were determined with the help of a pH meter (FP30-standard, Mettler Toledo, Switzerland).

2.4. Adsorption kinetics, isotherm, and thermodynamic performance of TNR@PEI–Zr

The adsorption performance of TNR@PEI–Zr was studied through a series of batch adsorption processes. About 10 mg of adsorbent was added to a 50 ml conical flask, and then 10 ml of the adsorbate solution with a known concentration (C_0, $mg{\cdot}L^{-1}$) was dispensed into the flask. The flask was then carefully sealed with hand-stretched film and tightly fixed with a rubber band at the neck of the flask. The conical flask was then placed in a thermostatic shaker at 120 $r{\cdot}min^{-1}$ at a constant temperature for a given time (t). After adsorption, the adsorbent was separated from the solution by centrifugation at 3000 $r{\cdot}min^{-1}$ and the residual concentration of the pollutant was measured on a visible spectrophotometry at the appropriate wavelengths (524 nm for Alizarin red and 700 nm using Mo–Tb anti spectrophotometry for phosphate).

The study of the various parameters influencing the adsorption processes was carried out as follows. The effects of pH (2–10), the effect of adsorbent dose (0.0025–0.05 g), the influence of contact time (0–350 min), the effect of temperature (293–313 K), the effect of adsorbate initial concentration at different temperatures (10–400 $mg{\cdot}L^{-1}$), and the effect of salts (NaCl, $NaHCO_3$, Na_2SO_4) at different concentrations (C_0, 0.02–1.0 $mol{\cdot}L^{-1}$).

The amount of pollutant adsorbed (q, $mg{\cdot}g^{-1}$) (Eq. (1)) and adsorbate removal efficiency (p, %) (Eq. (2)) were calculated by using the following formula.

$$q = \frac{V(C_0 - C)}{m} \tag{1}$$

$$p = \frac{C_0 - C}{C_0} \times 100\% \tag{2}$$

where C_0 and C ($mg{\cdot}L^{-1}$) are the initial and concentration at equilibrium or at any given time t, V (L) is the volume of solution, and m (g) is the mass of adsorbent.

The desorption efficiency (d, %) was evaluated using Eq. (3), while the regeneration efficiency (r) was also calculated using Eq. (4).

$$d = m_d/m_0 \times 100\% \tag{3}$$

$$r = q_r/q_e \times 100\% \tag{4}$$

where m_d (g) is the mass of adsorbate desorbed from the adsorbent, and m_0 (g) is the mass of adsorbate remaining on the adsorbent before desorption. r (%) is regeneration efficiency while q_r and q_e are the adsorption quantity of regenerative adsorbent for next recycle times and the initial adsorbent in the same experimental conditions, respectively.

The nonlinear forms of the kinetic and isotherm model equations used in this study are listed in Eqs. (5)–(12).

Pseudo-second-order kinetic model (PSO) [16]:

$$q_t = \frac{k_2 q_e^2 t}{1 + k_2 q_e t} \tag{5}$$

Elovich [17]:

$$q_t = A + B \ln t \tag{6}$$

Interparticle-diffusion model (IPD) [18]:

$$q_t = K_t t_{1/2} + C \tag{7}$$

Langmuir model [19]:

$$q_e = \frac{q_m K_L C_e}{1 + K_L C_e} \tag{8}$$

Separation factor:

$$R_L = \frac{1}{1 + K_L C_0} \tag{9}$$

Freundlich model [20]:

$$q_e = K_F C_e^{1/n} \tag{10}$$

Koble–Corrigan model [21,22]:

$$q_e = \frac{A C_e^n}{1 + B C_e^n} \tag{11}$$

where k_2 ($g{\cdot}mg^{-1}{\cdot}min^{-1}$) is the pseudo-second-order rate constant, q_t ($mg{\cdot}g^{-1}$) is the adsorption quantity at time t, q_e ($mg{\cdot}g^{-1}$) is the equilibrium adsorption capacity. A ($mg{\cdot}g^{-1}{\cdot}min^{-1}$) is a constant related to chemisorption rate and B ($g{\cdot}mg^{-1}$) is a constant which depicts the extent of surface coverage. K_t ($mg{\cdot}g^{-1}{\cdot}min^{-0.5}$) is the intraparticle diffusion rate constant, C is a constant that gives idea about the thickness of the boundary layer. q_m ($mg{\cdot}g^{-1}$) is the maximum adsorption capacity, K_L ($L{\cdot}mg^{-1}$) is a constant related to the affinity of the binding sites and energy of adsorption, R_L is separation factor, and that the adsorption system is regarded as favourable ($0 < R_L < 1$) or unfavourable ($R_L > 1$). K_F is the Freundlich constant related to the comparative adsorption capacity, and $1/n$ is the affinity of the adsorbate to the adsorbent. A and B are the Koble–Corrigan parameters.

To further elucidate the influence of temperature on the adsorption processes, the thermodynamic parameters such as change in free energy change (ΔG°) (Eq. (13)), enthalpy change (ΔH°) and entropy change (ΔS°) (Eq. (14)), and activation energy (E_a) (Eq. (15)) were determined.

$$K_c = C_{ad,e}/C_e \tag{12}$$

$$\Delta G^\circ = -RT \ln K_c \tag{13}$$

$$\Delta G^\circ = \Delta H^\circ - T\Delta S^\circ \tag{14}$$

$$\ln k_2 = \ln k_0 - \frac{E_a}{RT} \tag{15}$$

where K_c is the equilibrium constant and $C_{ad,e}$ ($mg{\cdot}L^{-1}$) is the concentration of the adsorbate on the adsorbent; R (8.314 $J{\cdot}mol^{-1}{\cdot}K^{-1}$) is the ideal gas constant, T (K) is the temperature of the reaction medium, k_2 is the pseudo-second order rate constant, k_0 is the temperature independent factor ($g{\cdot}mg^{-1}{\cdot}min^{-1}$).

2.5. Leaching test for TNR@PEI–Zr

In order to evaluate the stability of the engineered adsorbent under different pH values, 10 ml of distilled water was dispensed into 3 sets of conical flasks and the pH was adjusted to pH 2.0, 4.0, and 10.0 using drops of 0.1 $mol{\cdot}L^{-1}$ hydrochloric acid and sodium hydroxide. 10 mg of TNR@PEI–Zr was added to each flask and agitated in the thermostatic shaker at 313 K for 24 h. After filtering the solutions, the supernatant was used to determine the concentration of Zr following the standard methods described by El-Sayed *et al.* [23] using a UV–visible spectrophotometer at a wavelength of 331 nm against a reagent blank.

2.6. Statistical analysis

All experiments in this study were performed in triplicates and the means were used for the various calculations. With the help of Origin 6.0 professional and Microsoft excel 2016, the parameters of adsorption isotherm and kinetic data were calculated and the data pictorially graphed. An analysis to examine, compare and understand how the results obtained from experimental data fitted the various models tested, was achieved through the comparison of the coefficient of determination (R^2) (Eq. (16)), sum of squared estimate of error (SSE) (Eq. (17)), and chi-square statistics (χ^2)

$$R^2 = 1 - \mathrm{RSS/TSS} \tag{16}$$

$$\mathrm{SSE} = \sum_{i=1}^{n} (q_c - q_e)^2 \tag{17}$$

$$\chi^2 = \sum \frac{Q_i - E_i}{E_i} \tag{18}$$

where RSS is the sum of squares of residuals, TSS is the total sum of squares, n is the number of samples in a set of experiments, q_e and q_c represent the value obtained from the experiment and the value obtained from the model fitting. Q_i is observed value and E_i is the expected value.

3. Results and Discussion

3.1. Adsorbent characterization and structural analysis

3.1.1. Brunauer–Emmett–Teller analysis

The data for BET analysis on TNR@PEI–Zr is presented in Table 1. In the present study, TNR@PEI–Zr had a BET surface area of 2.43 $m^2 \cdot g^{-1}$ which is larger than that of its intermediate (TNR@PEI) reported in the earlier studies as well as other zirconium modified biosorbents [14,24]. The surface area of the adsorbent designed by Liu *et al.* [12] and Zhang *et al.* [25], on the other hand, was greater than that of TNR@PEI–Zr. Because of the relatively small surface area of TNR@PEI–Zr, it can be inferred that physisorption was not the only factor mediating the efficient adsorption of AR and PO_4^{3-}, but chemisorption through zirconium complexation might have also played a role in the adsorption systems of both AR and PO_4^{3-} [12]. There was a slight decrease in the average pore radius and a substantial rise in the pore volume. The reduction in the surface area and average pore radius could be attributed to the plugging of the pores on the TNR@PEI–Zr by the incorporated zirconium metal [12,24,26].

3.1.2. SEM spectroscopy analysis

The SEM micrographs at different magnifications provided useful information on the surface structure of the engineered adsorbent. SEM images displayed in Fig. 1 presents a well-developed pore channel of varying sizes and shapes. These porous structures are beneficial for the increase of adsorptive capacity of the adsorbent. These well-developed pores have been proved to be areas where pollutants could easily be trapped during the adsorption process.

Table 1
Microstructure parameters of TNR and TNR@PEI–Zr

Textural properties	TNR[①]	TNR@PEI–Zr
BET surface area/$m^2 \cdot g^{-1}$	0.319[①]	2.43
BET total pore volume/$cm^3 \cdot g^{-1}$	0.000272[①]	0.00158
BET pore size/nm	3.42[①]	2.27

[①] Data extracted from Ref. [8].

Such adsorbent surface property greatly enhanced may have played key role in the efficient removal of alizarin red and phosphate. The honeycomb-like pore structures were absent from the pristine TNR. It can therefore be intimated that the engineering process is responsible for the porous structure of the TNR@PEI–Zr.

3.1.3. Fourier-transform infrared spectroscopy analysis

The FTIR spectra of the engineered adsorbent are displayed in Fig. 2(a). Generally, the modifications resulted in some new peaks appearing and some other peaks being diminished and or shifted in position in the engineered adsorbent. The stretching and bending vibration of —OH functional group and molecular H_2O at 3412 cm^{-1} of TNR shifted to 3416 cm^{-1} in the case of TNR@PEI and TNR@PEI–Zr. The existence of a broad and strong band extending from 3200 to 3600 cm^{-1} is linked with overlapping O—H and N—H stretching, which might be attributable to the presence of an NH_2 functional group on the TNR@PEI surface. The presence of hydroxyl and amine groups on the TNR@PEI surface is verified by the presence of alcoholic C—O and C—N stretching vibrations at 1115 and 1161 cm^{-1} [15]. These confirm the successful modification of the pristine TNR with PEI. The vibration peaks at 2924 and 2854 cm^{-1} on TNR were maintained in TNR@PEI but whiles the peak at 2924 cm^{-1} shifted slightly to 2923 cm^{-1}, the peak at 2854 cm^{-1} disappeared on TNR@PEI–Zr spectrum. These bands are associated to the asymmetric and symmetric stretching vibration of C—H, from the —CH, —CH_2, —CH_3 methylene chains [27].

The peak at 1640 cm^{-1} on TNR which reappeared at 1632 cm^{-1} on TNR@PEI and 1636 cm^{-1} on TNR@PEI–Zr can be attributed to the C=C/C=O stretching vibrations of alkene/carboxyl groups [27]. The peak at 1510 cm^{-1} on the TNR@PEI–Zr is associated with Zr—OH bonds [28]. The bending vibration of Zr—OH groups can be ascribed to the band at 1373 cm^{-1} [29]. The peak at 1046 cm^{-1} may be attributed to Zr—OH vibration. The characteristic peak observed at 841 cm^{-1} is ascribed to Zr—O—C vibration [30]. In addition, the band at 515 cm^{-1} which is due to stretching vibrations of Zr—O and the weak peak at 464 cm^{-1} which is related to ZrO_2 and Zr=O, further confirms that zirconium atoms were present on the surface of the adsorbent [9].

3.1.4. X-ray diffraction analysis

The XRD patterns of TNR, TNR@PEI and TNR@PEI–Zr are presented in Fig. 2(b). The characteristic peaks of a well-structured crystalline cellulose at 22.57° and 34.27° were present in both the TNR and the TNR@PEI. However, the engineering of TNR@PEI–Zr had transformed TNR into a complete amorphous structure as the peak at 34.27° had disappeared and the intensity of peak 22.57° had drastically diminished from 6500 to below 2000.

3.1.5. X-ray photoelectron spectroscopy analysis

The XPS analysis was conducted to analyse the modification in the surface chemistry of the precursor and the engineered adsorbent before and after pollutant decontamination whose images are presented in Fig. 3. The XPS survey spectra of TNR@PEI–Zr before (Fig. 3(a)) and after adsorptive removal of AR (Fig. 3(b)) and phosphate (Fig. 3(c)) indicate the appearance of new peaks (S 2p and P 2p), indicative of the presence of AR and PO_4^{3-} on the adsorbent surface. Comparing the XPS survey of TNR and TNR@PEI as reported in earlier to that in Fig. 3(a), a characteristic peak of zirconium is detected at 183.0 eV which is a demonstration of the successful loading of Zr(IV) on the adsorbent surface. There are also some slight shifts and changes in the intensities of the peak positions of C 1s, N 1s, O 1s and Zr 3d. For example, the peak intensities of C 1s on TNR@PEI–Zr (Fig. 3(d)) had reduced significantly after AR (Fig. 3(e)) and PO_4^{3-} (Fig. 3(f)) adsorption. A similar trend is

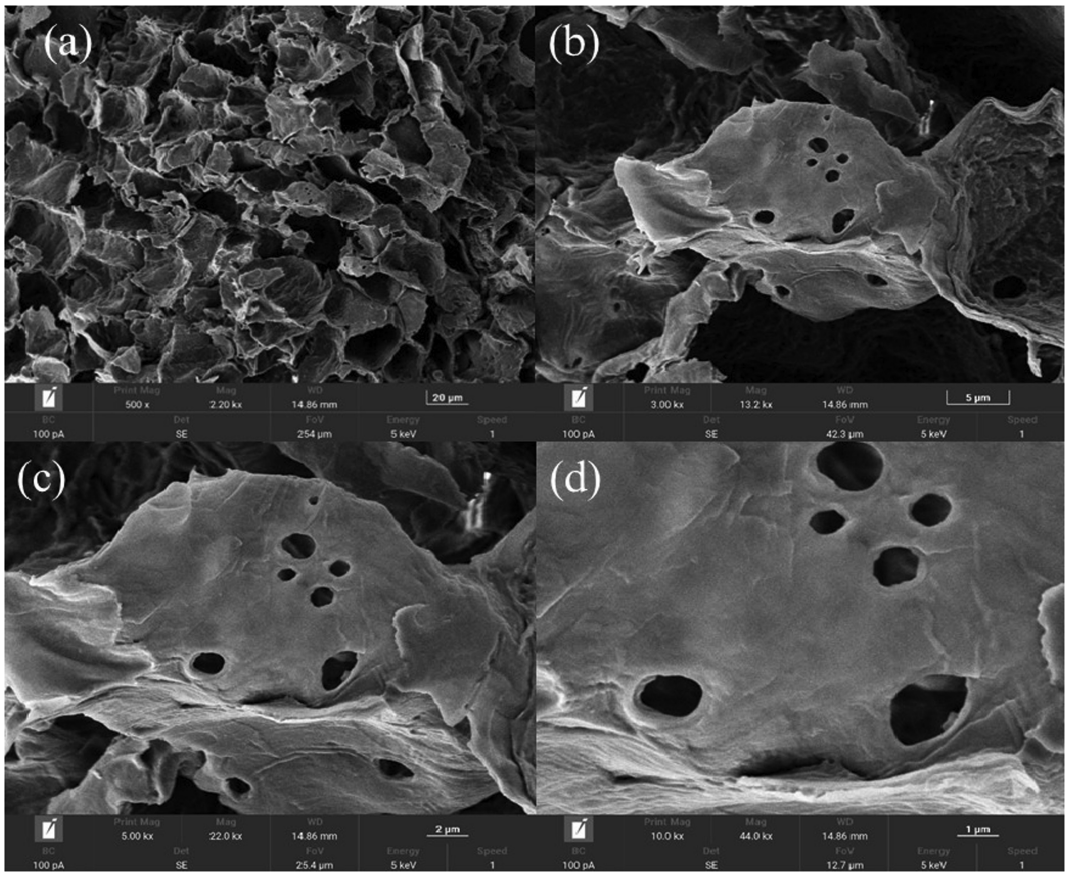

Fig. 1. SEM images of TNR@PEI–Zr at (a) 20 μm, (b) 5 μm, (c) 2 μm and (d) 1 μm.

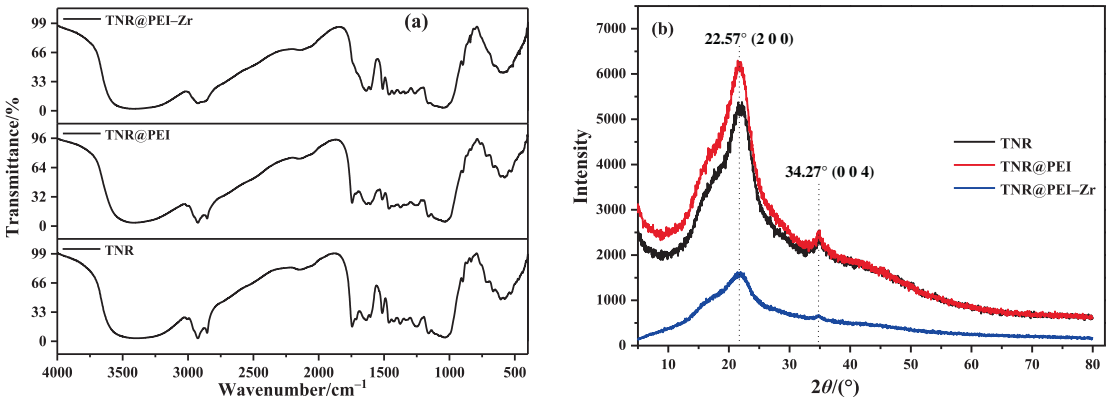

Fig. 2. (a) FTIR spectra and (b) XRD patterns of the engineered TNR@PEI–Zr and its precursor.

observed in the O 1s as depicted in Fig. 3(g), (h) and (i). The proportional increase of O 1s from 19.9% in TNR@PEI–Zr to 21.1% in TNR@PEI–Zr–AR and 24.2% in TNR@PEI–Zr–PO_4^{3-}, indicating a percentage increase in metal oxygen which is accordant with the outcome of the formation of Zr—O bonds is suggestive of the important role of Zr in the adsorptive uptake of AR and PO_4^{3-}. It is obvious that the four peaks around 529.5, 530.8, 531.8, 532.1, and 533.7 eV are the typical peaks of O 1s, related to Zr—O, C—O/O^{2-}, O—H/Zr—O, C—O/O—H/P—O—P and O—H bonding, respectively [12,31–33]. In addition, the proportional increase in the deconvoluted peaks of Zr—O and C—O/O^{2-} after AR and PO_4^{3-} removal may suggest the critical role Zr played in the complexation removal of these pollutants. Moreover, the Zr—O and O—H/Zr—O bindings in TNR@PEI–Zr–AR and TNR@PEI–Zr–PO_4^{3-} indicated that the adsorption reaction mechanism comprised complexation between Zr and —OH in AR and PO_4^{3-} [12,32]. In the high-resolution XPS spectrum of N 1s (Fig. 3(j), (k), and (l)), TNR@PEI–Zr contained a C—N at peak 398.8 eV which was absent after the adsorption of AR and the peaks at 397.7 eV and 398 eV also disappeared after the adsorption of PO_4^{3-}. Also, the peak at 397.7 eV had shifted to 396.3 eV. The significant reduction in the intensities of the peaks is all suggestive of their participation in the removal of the pollutants. The 4 peaks in Fig. 3(m) had reduced to 3 in Fig. 3(n) and 2 in Fig. 3(o). The presence of Zr on the Fig. 3(m) at peaks 179.1 eV (Zr—C), 181.9 eV (Zr—H), 182.3 eV (Zr=C/ZrO_2) and 184.5 eV (Zr—N) corresponds to the Zr $3d_{5/2}$ and Zr $3d_{3/2}$ peaks of Zr(IV) indicative of the successful incorporation of Zirconium into the biosorbent [31,34]. The involvement of Zr in the removal

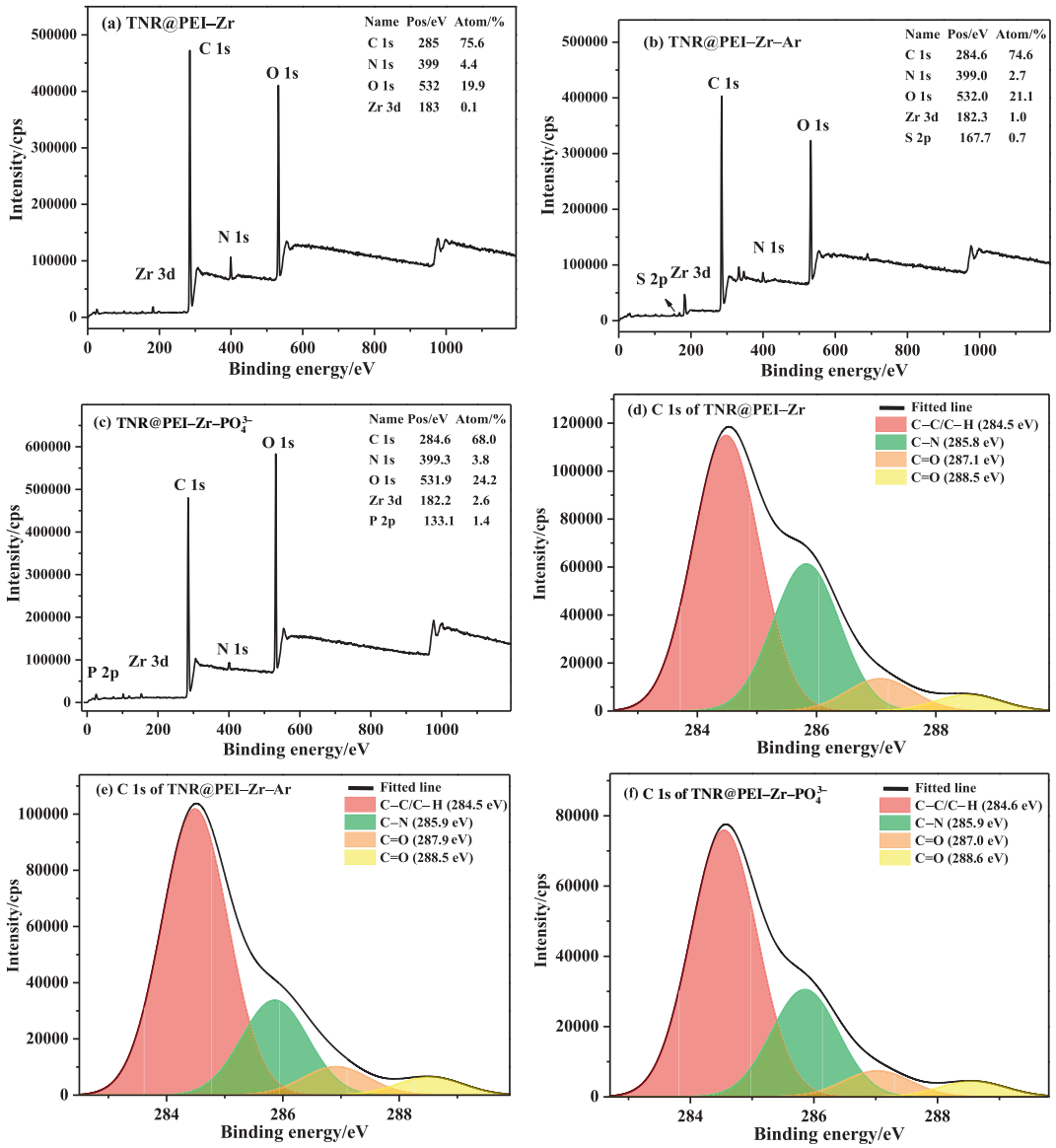

Fig. 3. Full XPS spectra of TNR@PEI–Zr (a), TNR@PEI–Zr–Ar (b), TNR@PEI–Zr–PO_4^{3-} (c). Typical high resolution XPS spectra of C 1s (d, e, f), N 1s (g, h, i), O 1s (j,k,l) and Zr 3d (m, n, o) of TNR@PEI–Zr, TNR@PEI–Zr–Ar and TNR@PEI–Zr–PO_4^{3-} respectively. Deconvolution of S 2p of TNR@PEI–Zr–Ar (p) and P 2p of TNR@PEI–Zr–PO_4^{3-} (q).

of AR is confirmed from the new peak appearing at 185.0 eV (Zr—O) and the coordination of Zr with PO_4^{3-} is observed in the peaks at 182.2 eV (Zr—O) and 184.6 eV (Zr—O). After the removal of AR, a new binding peak of S 2p is recorded at 167.7 eV (Fig. 3 (b)) and deconvoluted into 167.5 eV (S═O), 168.4 eV (S═O_2) and 169.3 eV (—SO_3—C—) (Fig. 3(p)) [35,36]. These observations suggest the presence of AR molecules on TNR@PEI–Zr surface [12]. The appearance of P 2p peak of phosphate (Fig. 3(c)) confirms the presence of phosphate and is deconvoluted into four components: polyphosphates (132.3 eV), pyrophosphate P—O—P linkage (132.9 eV), tetra-coordinated pentavalent phosphorus as in phosphates (133.7 eV), and metaphosphates PO_3^- (134.5 eV) [37]. This indicates the successful adsorption of phosphate unto the TNR@PEI–Zr.

3.2. Adsorption study

3.2.1. pH zero point charge and effect of initial pH

TNR@PEI–Zr presented a pH zero point charge (pH_{zpc}) of 6.7 in Fig. 4(a) whereas the unmodified TNR and TNR@PEI recorded pH_{zpc} of 5.5 and 7.0. The presence of pyridine and use of $ZrOCl_2{\cdot}8H_2O$ might be responsible for the change in the pH_{zpc}. These observed changes in the pH_{zpc} are indicative of the surface modification of the precursor TNR. The cationic surface obtained by TNR@PEI–Zr at pH below 6.7 results in a strong attraction between the anions of AR and PO_4^{3-}. This explains why adsorption was highest in acidic medium and drastically reduced in the alkaline medium from pH 6 to 10 as the positively charged surfaces begun to decrease. This is because the surface charge of TNR@PEI–Zr is positive when solution pH is below the pH_{zpc}. This positive surface is ideal for the removal of the negatively charged AR and PO_4^{3-} ions. The reduced adsorption observed in pH above the pH_{zpc} is due to the barrier created because of the electrostatic repulsion interaction existing between the negatively charged anions of Alizarin red and phosphate which results in the inhibition of AR and PO_4^{3-} adsorption onto the negatively charged surface of the adsorbent [38]. Understanding the pH effect of adsorption process is important as change in the solution pH has a direct consequence on the possible ion–ion interactions that may exist between the charged surface of the adsorbent material and the adsorbate molecules. The pK_a value of diprotic AR is

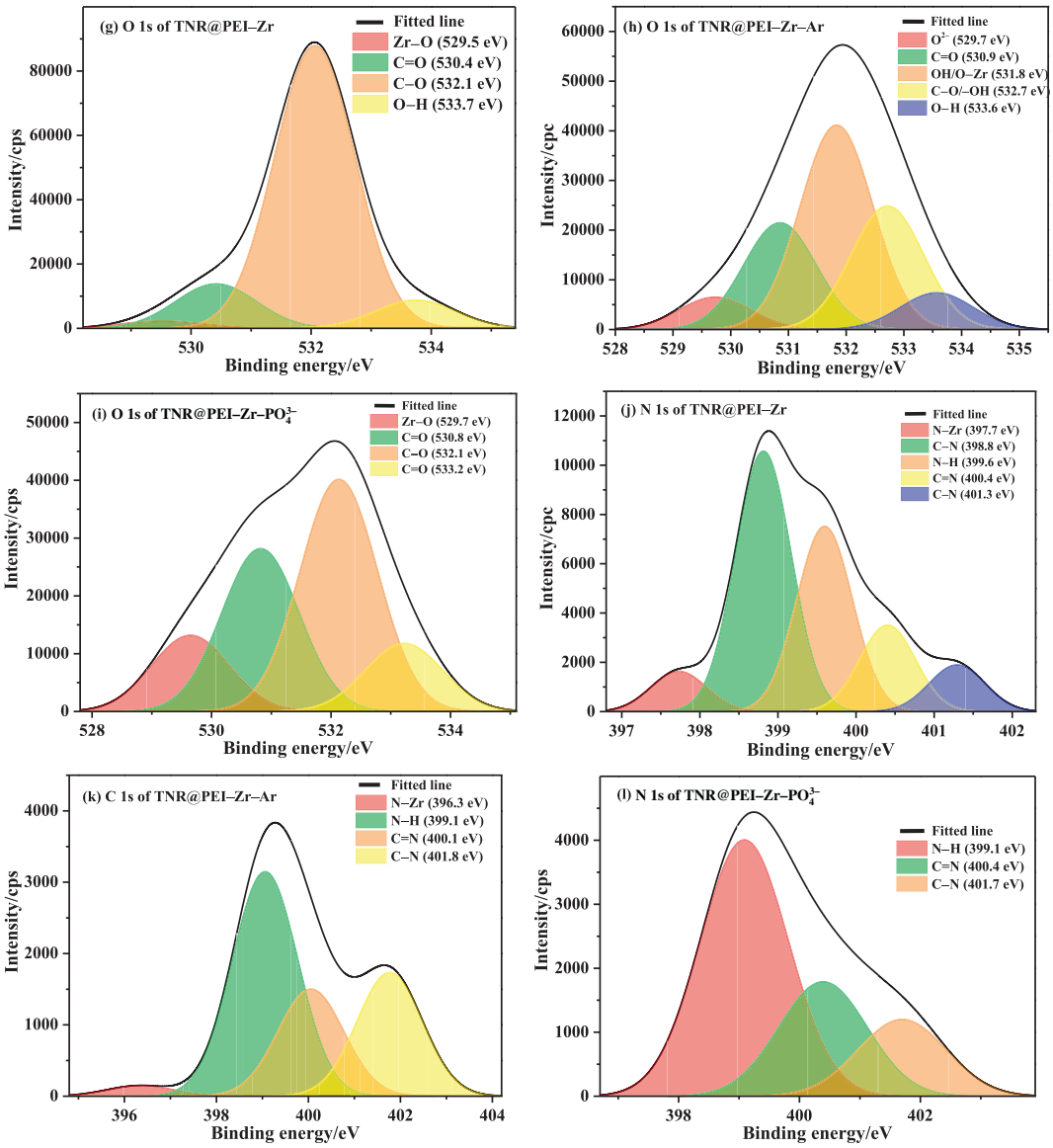

Fig. 3 (*continued*)

reported to be 5.82 and 10.78 [39] whiles that of PO_4^{3-} is 2.12, 7.21 and 12.32 at 293 K for $H_2PO_4^-$, HPO_4^{2-}, and PO_4^{3-} respectively.

In the investigated pH range (2–10) for AR and (2–12) for PO_4^{3-} a very strong dependency of AR and phosphate removal by TNR@PEI–Zr was observed as reported in Fig. 4(b) and (c). The pH of the engineered adsorbent subsisted in the protonated form at solution pH between 2 and 6 due to the ionization of functional groups of the adsorbent. There was a substantial electrostatic attraction between the positively charged adsorbent surfaces and the negatively charged anionic Alizarin red and phosphate. This explains the high adsorption capacity recorded in acidic medium. On the other hand, as pH rises from 6 to 10 and 12, a sharp decrease in adsorption capacity of TNR@PEI–Zr towards AR and PO_4^{3-} is observed. The presence of high amount of hydroxonium (OH^-) ions competes against the active sites on the TNR@PEI–Zr surface. The ideal pH for the adsorption of AR and PO_4^{3-} ranged between 2–5 and 2–6 respectively, with a very small difference in the adsorption capacity in that range, hence, a pH of 3 was used in the ensuing experiments [7,40].

3.2.2. Effect doze on the adsorption performance of TNR@PEI–Zr

Since the mass of applied adsorbent is inversely proportional to the number of accessible binding sites during the adsorption process, the adsorbent dosage typically affects the adsorption process. Therefore, the optimal adsorbent dosage should display adequate adsorption capacity at the given dose in addition to good removal efficiency. Examining the dose effect can assist in determining how efficient and effective an adsorbent is when taking into account its cost-effectiveness for use and its capacity to cleanse the pollutant at a low dosage.

The removal effectiveness of AR and PO_4^{3-} increases with an increase in adsorbent dosage from 0.005 to 0.05 g and 0.0025 to 0.04 g, respectively, according to Fig. 5(a) and (b). However, the removal efficiency virtually approached equilibrium and an adequate adsorption capacity had been established beyond a dosage of 0.010 g. On the other hand, if the dose is increased, TNR@PEI–Zr's capacity for adsorption declines. These startling findings are the consequence of a rise in surface area and the number of accessible adsorption sites for the fixed number of adsorbate molecules

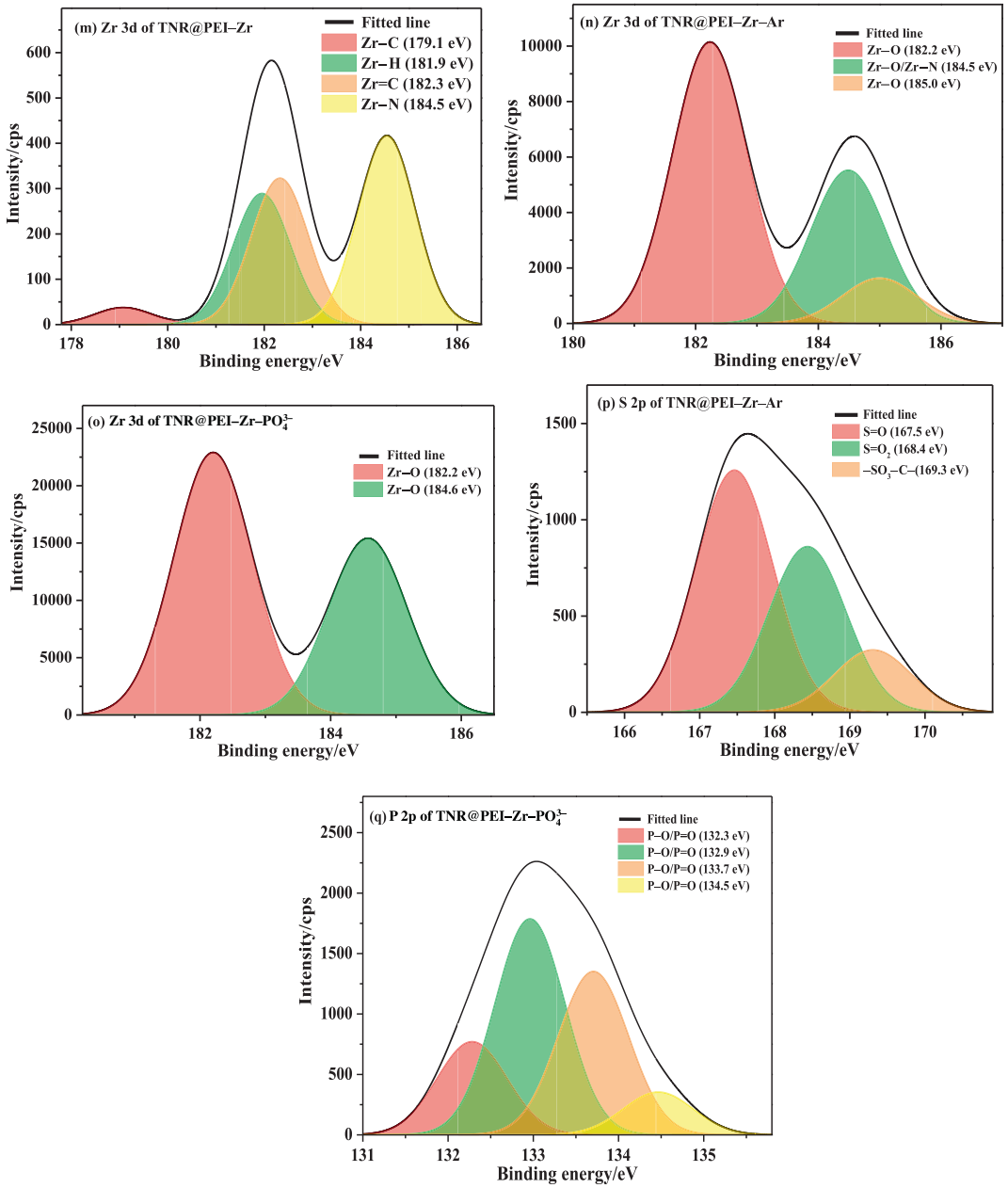

Fig. 3 (*continued*)

as well as the underutilisation of available binding sites, which leads to unsaturation of the active sites on the biosorbent. At a dosage of 0.01 g, the percentage efficiency and q_e were 192.6 mg·g^{-1} and 96.3% for AR and 27.6 mg·g^{-1} and 91.9% for PO_4^{3-}, respectively. Hence the effective dose used for subsequent experiments was 0.01 g of TNR@PEI–Zr. This performs better than the adsorptive capacity of the adsorbent reported by Dovi *et al.* [7] towards PO_4^{3-} and that of Aryee *et al.* [14], Adeogun and Babu [41], and Slimani *et al.* [42] for AR.

3.2.3. Effect of ionic strength

To establish the efficiency and performance of an adsorbent for practical application in the wastewater remediation process, it is exigent to investigate the possible effect of coexisting ions on the adsorptive capabilities of the adsorbent. Thus, the effects of Cl^-, HCO_3^-, and SO_4^{2-} at different concentrations (0.02–1.0 mol·L^{-1}) and optimum experimental conditions were examined on the adsorption of AR and PO_4^{3-} by TNR@PEI–Zr, and the results are illustrated in Fig. 5(c) and (d). The results show that the adsorptive capability of TNR@PEI–Zr diminished in the presence of the ions tested for both AR and PO_4^{3-}. A similar trend was observed for the reduced adsorption potential in AR and PO_4^{3-} (HCO_3^- > SO_4^{2-} > Cl^-). This observation could be explained by the fact that there existed some competition between the ions of the salt and the available active sites on the adsorbent, causing electrostatic repulsion between the anionic dye and negatively charged phosphate ions. This confirms the key role electrostatic interactions played in the removal of AR and PO_4^{3-} by TNR@PEI–Zr. Nonetheless, Pap *et al.* [43] posited that it is quite improbable that the effluent from a secondary wastewater treatment process will present all these anions at concentrations high enough to result in such profound declines in the AR and PO_4^{3-} adsorption capacity. That

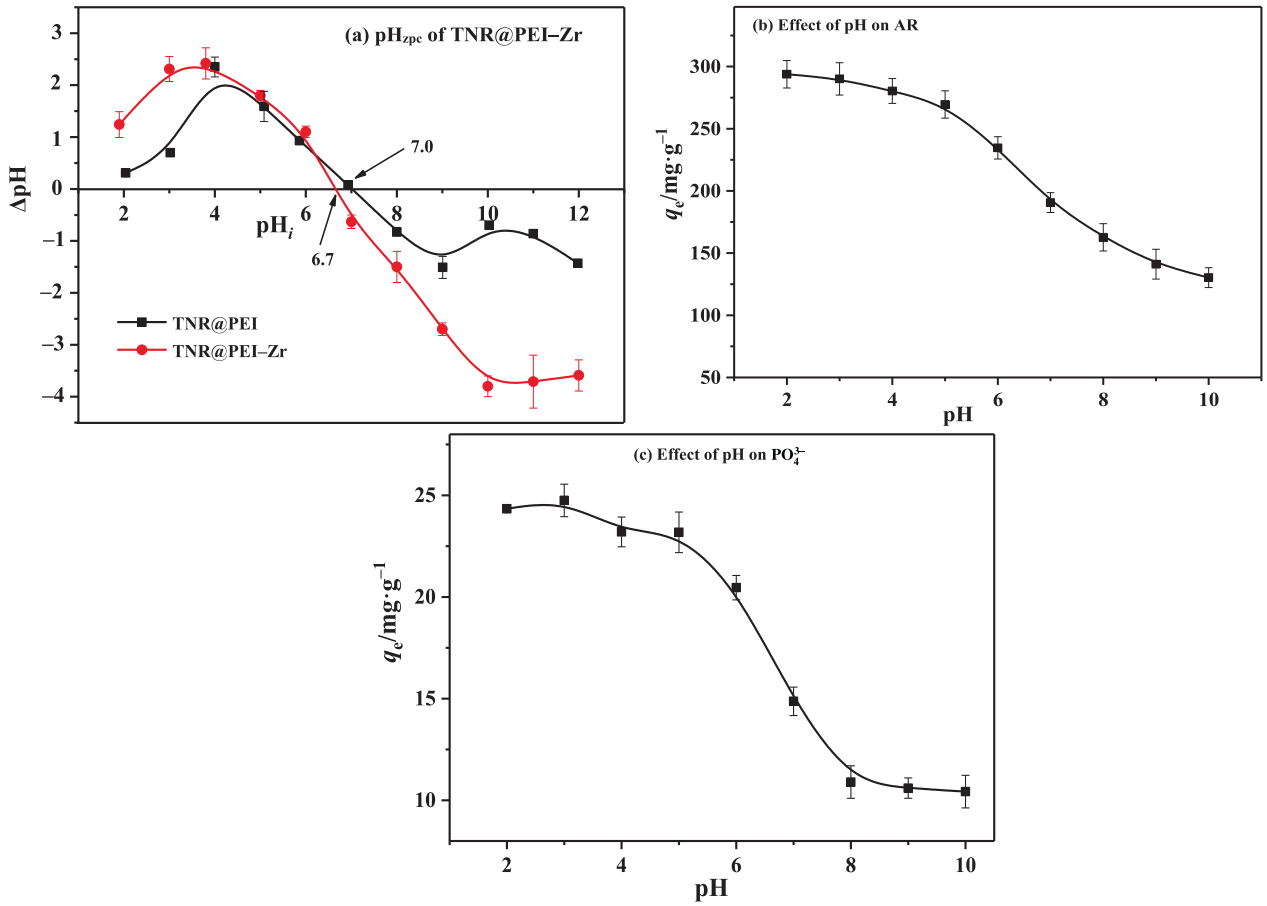

Fig. 4. pH point of zero charge of TNR@PEI–Zr (a). Effects of initial ph on adsorption of AR (C_0 = 200 mg·L^{-1}, m = 1 g·L^{-1}, t = 2 h, T = 313 K) (b) and PO_4^{3-} (C_0 = 30 mg·L^{-1}, m = 1 g·L^{-1}, t = 2 h, T = 313 K) (c).

notwithstanding, the fact that the adsorption capacity of TNR@PEI–Zr was still noticeable even at a high salt concentration supports the claim that other factors in addition to electrostatic interactions might be contributing to mechanisms mediating the removal of Alizarin red and phosphate by TNR@PEI–Zr.

3.2.4. Contact time effects and kinetic modelling

Time-dependent sorption studies were used to examine the adsorption kinetics in order to comprehend the mechanism underlying the removal of TNR@PEI–Zr toward AR and PO_4^{3-}. The effect of time and kinetic modelling of PSO, Elovich, and IPD are shown in Fig. 6(a) for AR and Fig. 6(b) for PO_4^{3-}. The kinetic curve may be split into two parts, the first of which is the initial fast adsorption phase, during which over 90% of the pollutants are adsorbed as a result of the abundance of binding sites on the adsorbent surface and the high concentration of the pollutant in solution. As the reaction advances, the second phase is characterised by a slower rate of uptake, and equilibrium is eventually reached at around 50 min for AR and 60 min for PO_4^{3-}.

The kinetic curve can be divided into two phases, the first being the initial rapid adsorption within which over 90% of the pollutants are adsorbed due to the availability of abundant binding sites on the adsorbent surface coupled with the high concentration of the pollutant in solution. The second phase is characterised by a reduced rate of uptake as the reaction progresses until equilibrium is achieved at about 50 min for AR and 60 min for PO_4^{3-}. This is largely because the active binding sites on the surface of the adsorbent decreased with time, which resulted in a reduced rate of adsorption until reaching a point where the removal rate was not significant as the vacant spaces were already filled. It is also observed that an increase in temperature was favourable to the adsorption of both AR and PO_4^{3-} suggestive of an endothermic process.

The kinetic curve can be divided into two phases, the first being the initial rapid adsorption within which over 90% of the pollutants are adsorbed due to the availability of abundant binding sites on the adsorbent surface coupled with the high concentration of the pollutant in solution. The second phase is characterised by a reduced rate of uptake as the reaction progresses until equilibrium is achieved at about 50 min for AR and 60 min for PO_4^{3-}. This is largely because the active binding sites on the surface of the adsorbent decreased with time, which resulted in a reduced rate of adsorption until reaching a point where the removal rate was not significant as the vacant spaces were already filled. It is also observed that an increase in temperature was favourable to the adsorption of both AR and PO_4^{3-} suggestive of an endothermic process.

The kinetic parameters obtained by the model fitting are listed in Table 2a for AR and Table 2b for PO_4^{3-}. The best model fitting based on the highest coefficient of determination (R^2), the least squared error approximation (SSE) and a relatively smaller chi-square statistics (χ^2) values suggests PSO to better fit the kinetics process for both AR and PO_4^{3-}. Moreover, the values of q_e calculated from PSO models at temperatures of 293, 303, and 313 K (165.7, 186.5, and 204.9 mg·g^{-1} for AR and 24.4, 29.1, and 31.3 mg·g^{-1} for PO_4^{3-}) are very similar to the experimentally observed values (155.7, 178.0, and 198.8 mg·g^{-1} for AR and 17.4, 23.3, and 27.7 mg·g^{-1} for PO_4^{3-}). The results of the experimental data and model fitting show that the engineered adsorbent is more effective in removing AR than

PO_4^{3-}. However, the kinetic constant (k_2) values confirmed that the adsorption process for PO_4^{3-} (k_2 = 6.07 × 10^{-4}, 7.64 × 10^{-4}, and 13.40 × 10^{-4} g·mg^{-1}·min^{-1}) was faster than that of AR (k_2 = 3.25 × 10^{-4}, 3.40 × 10^{-4} and 4.92 × 10^{-4} g·mg^{-1}·min^{-1}).

3.2.5. Effects of equilibrium concentration and isotherm fitting

In order to study the adsorption pathway and equilibrium relationship between the engineered adsorbent and AR and PO_4^{3-}, nonlinear isotherm modelling of Langmuir, Freundlich, and Koble–Corrigan, were investigated to predict the appropriate parameters and behaviour of TNR@PEI–Zr towards the different pollutant adsorption systems. The fitted isothermal plots for AR and PO_4^{3-} at different temperatures (293, 303, and 313 K) are shown in Fig. 6(c) and (d), while the relevant model parameters are presented in Tables 3a and 3b respectively. The adsorption of AR resulted in a rapid increase in q_e between the initial equilibrium concentration of 1.64 and 26 mg·L^{-1}, whereas the adsorption of PO_4^{3-} resulted in a sharp increase in q_e between 0.356 and 20.6 mg·L^{-1}. This initial sharp increase was followed by a slower adsorption stage until equilibrium was reached, as adsorption capacity tended to be stable [27].

The experimental data were further fitted by the Langmuir, Freundlich and Koble–Corrigan models and their parameters are shown in Tables 3a and 3b for AR and PO_4^{3-}, respectively. Koble–Corrigan and Langmuir models show good agreement with the experimental results based on the high R^2, low SSE and the least χ^2 values. A good fit with the Koble–Carrigan model is suggestive of the incorporation of both Langmuir and Freundlich isotherms and that at high adsorbate concentrations, the model reduces to a Freundlich isotherm and behaves as Langmuir at low concentrations of the adsorbate. However, the Koble–Carrigan model is incapable of defining the experimental data at all the studied temperatures for both pollutants under study in this work because some of the "*n*" values in Tables 3a and 3b are less than unity (1). Koble–Carrigan model is only valid when the constant "*n*" is greater than or equal to 1 [8] despite high concentration coefficient or SSE values.

The experimental data agrees well with the Langmuir model. A good and favourable Langmuir fit suggests a monolayer of adsorbates were formed on the TNR@PEI–Zr surface and that the adsorption sites on the surface of the adsorbent are uniform with a maximum adsorption capacity of 537.8 mg·g^{-1} for AR and 100.5 mg·g^{-1} for PO_4^{3-} at a temperature of 313 K. The favourability of these adsorption systems is confirmed by the values of the separation factor (R_L) as listed in Tables 3a and 3b. The values of R_L were 0.14, 0.11, and 0.03 for AR and 0.40, 0.33, and 0.37 for PO_4^{3-} at 293, 303, and 313 K. All the R_L values were within the range of 0–1.0, indicating the highly efficient adsorption of AR and PO_4^{3-} onto the TNR@PEI–Zr surface is favourable. Furthermore, the values of R_L seem to confirm the endothermic nature of the adsorption system of AR and PO_4^{3-} since increasing temperature favours the adsorption process. Moreover, considering the model parameters from the Freundlich isotherm, all the values of 1/*n* being less than unity, suggest a good and favourable adsorption system for both AR and PO_4^{3-}. The endothermic nature of both AR and PO_4^{3-} adsorp-

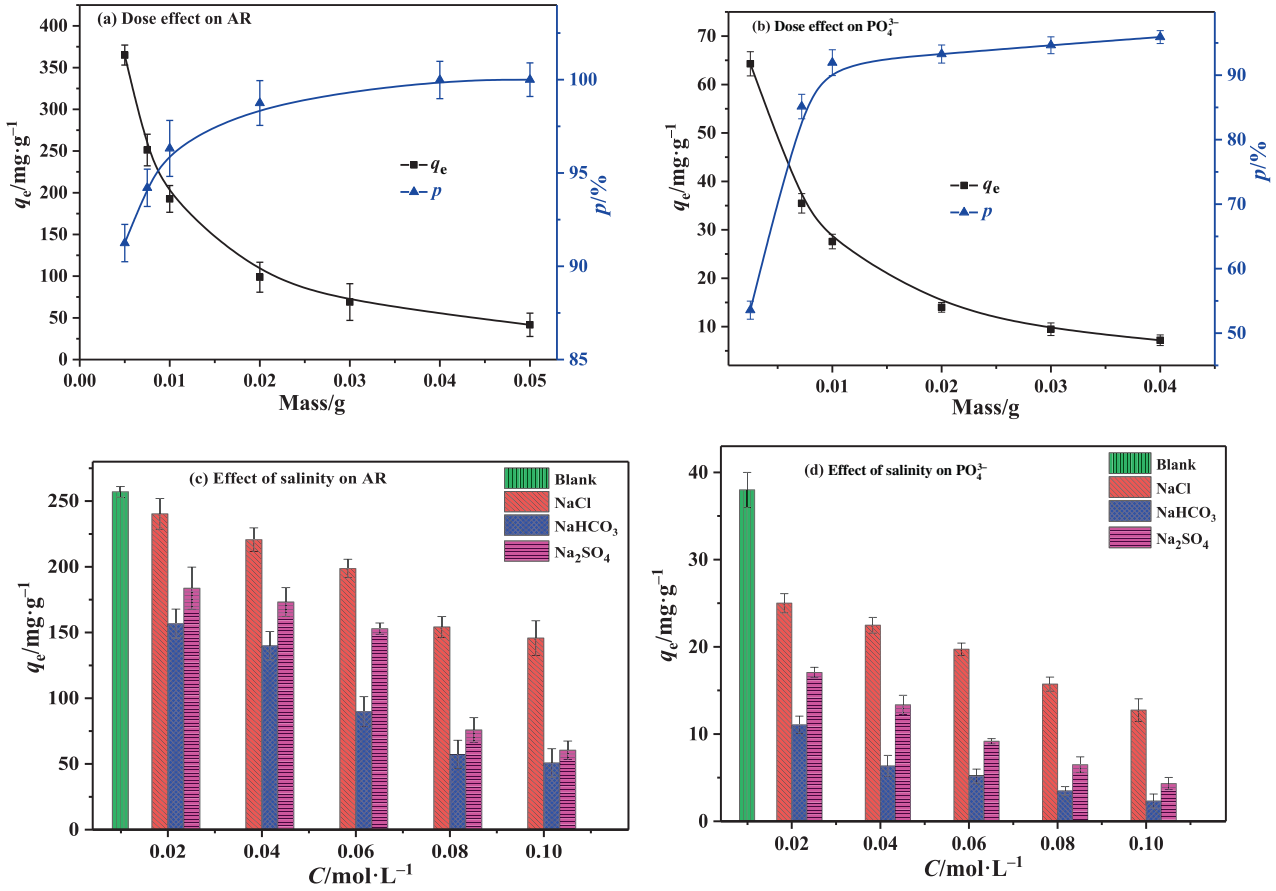

Fig. 5. Effects of adsorbent dozes on AR (C_0 = 200 mg·L^{-1}, t = 2 h, T = 313 K, pH = 3) (a), PO_4^{3-} (C_0 = 30 mg·L^{-1}, t = 2 h, T = 313 K, pH = 3) (b), effects of salts on AR (C_0 = 200 mg·L^{-1}, t = 2 h, T = 313 K, pH = 3, m = 1 g·L^{-1}) (c) and PO_4^{3-} (C_0 = 30 mg·L^{-1}, t = 2 h, T = 313 K, pH = 3, m = 1 g·L^{-1}) (d).

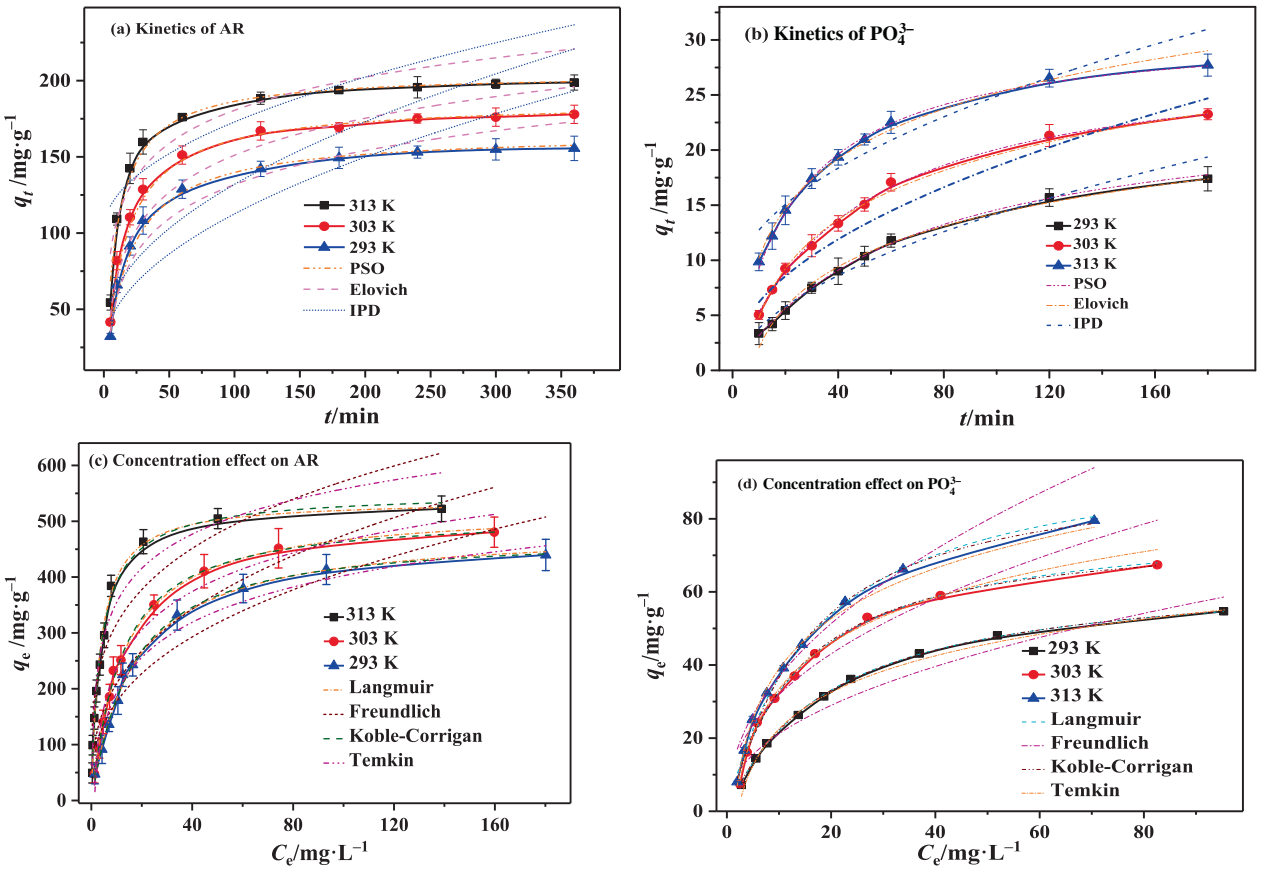

Fig. 6. Effects of time and kinetic modelling on the adsorption of AR (C_0 = 200 mg·L^{-1}, pH = 3, m = 1 g·L^{-1}) (a), PO_4^{3-} (C_0 = 30 mg·L^{-1}, pH = 3, m = 1 g·L^{-1}) (b), equilibrium concentration and isotherm modelling of AR (pH = 3, m = 1 g·L^{-1}, t = 2 h) (c), and PO_4^{3-} (pH = 3, m = 1 g·L^{-1}, t = 2 h) (d) onto TNR@PEI–Zr.

tion unto TNR@PEI–Zr is further confirmed by the values the Freundlich model adsorption index (K_F) [27].

3.3. Thermodynamic studies

Usually, a dimensionless equilibrium constant can be considered to calculate the thermodynamic parameters [44]. In this study, the constant K_c in Eq. (12) was applied. The effect of temperature variation on the adsorption capacity of TNR@PEI–Zr was studied, and the thermodynamic parameters calculated are listed in Table 4. From the enthalpy change ($\Delta H°$) values as presented in Table 4, the adsorption systems were temperature dependent, as higher temperatures resulted in increased adsorption capacities towards AR and PO_4^{3-}. This observation confirms the endothermic nature of the overall adsorption process. The adsorption process of AR may be largely mediated by chemisorption based on the value of ($\Delta H°$) (62.1 kJ·mol^{-1}) which is more than 40 kJ·mol^{-1}, while physisorption dominates that of PO_4^{3-}. The small values of

Table 2a
Kinetic parameters of AR adsorption onto TNR@PEI–Zr at different temperatures

	293 K	303 K	313 K
PSO			
q_e/mg·g^{-1}	165.7 ± 3.5	186.5 ± 2.9	204.9 ± 2.4
$k_2 \times 10^4$/g·mg^{-1}·min^{-1}	3.25 ± 0.27	3.40 ± 0.24	4.92 ± 0.44
R^2	0.994	0.995	0.987
SSE	6.36	8.64	11.60
χ^2	0.795	1.080	1.450
Elovich			
A	−16.6 ± 5.5	−10.3 ± 7.1	36.1 ± 17.0
B	32.3 ± 1.7	32.2 ± 1.7	31.4 ± 3.8
R^2	0.974	0.973	0.881
SSE	25.9	48.3	104.0
χ^2	3.24	6.04	13.02
IPD			
K_t	8.99 ± 1.3	9.90 ± 1.3	7.10 ± 1.8
C	22.7 ± 9.9	33.0 ± 11.8	101.9 ± 18.8
R^2	0.836	0.861	0.628
SSE	166	245	325
χ^2	20.68	30.67	40.59

Table 2b
Kinetic parameters of PO_4^{3-} adsorption onto TNR@PEI–Zr at different temperatures

	293 K	303 K	313 K
PSO			
q_e/mg·g^{-1}	24.4 ± 0.6	29.1 ± 0.4	31.3 ± 0.4
$k_2 \times 10^4$/g·mg^{-1}·min^{-1}	6.07 ± 0.41	7.64 ± 0.30	13.4 ± 0.8
R^2	0.998	0.999	0.996
SSE	0.589	1.641	1.270
χ^2	0.084	0.234	0.181
Elovich			
A	−10.1 ± 0.8	−10.0 ± 0.4	−4.83 ± 0.86
B	5.30 ± 0.21	6.42 ± 0.10	6.52 ± 0.23
R^2	0.988	0.998	0.991
SSE	3.02	2.15	3.02
χ^2	0.431	0.343	0.432
IPD			
K_t	1.52 ± 0.10	1.80 ± 0.13	1.78 ± 0.23
C	−0.983 ± 0.710	0.486 ± 0.760	7.120 ± 1.720
R^2	0.965	0.961	0.882
SSE	8.56	45.18	37.59
χ^2	1.22	6.45	5.37

Table 3a
Parameters of adsorption isotherms models for AR adsorption onto TNR@PEI–Zr at different temperatures

	293 K	303 K	313 K
Langmuir			
$q_{m\ (exp)}$/mg·g^{-1}	439.6 ± 28.0	480.4 ± 27.1	522.3 ± 23.1
$q_{m\ (theo)}$/mg·g^{-1}	486.9 ± 10.8	525.5 ± 9.5	537.8 ± 13.2
K_L/L·mg^{-1}	0.060 ± 0.003	0.079 ± 0.004	0.283 ± 0.024
R_L	0.14	0.11	0.03
R^2	0.995	0.997	0.990
SSE	1.61	1.17	6.35
χ^2	0.202	0.146	0.794
Freundlich			
K_F	76.1 ± 12.2	92.3 ± 16.8	174.5 ± 24.6
$1/n$	0.365 ± 0.04	0.356 ± 0.05	0.258 ± 0.04
R^2	0.908	0.876	0.854
SSE	27.5	45.3	91.4
χ^2	3.43	5.67	11.40
Koble–Corrigan			
A	25.99 ± 4.26	36.95 ± 3.42	165.0 ± 13.9
B	0.055 ± 0.008	0.072 ± 0.006	0.298 ± 0.026
n	1.05 ± 0.08	1.07 ± 0.05	0.898 ± 0.076
R^2	0.994	0.997	0.991
SSE	1.52	0.920	5.11
χ^2	0.216	0.131	0.730

Table 3b
Parameters of adsorption isotherms models for PO_4^{3-} adsorption onto TNR@PEI–Zr at different temperatures

	293 K	303 K	313 K
Langmuir			
$q_{m\ (exp)}$/mg·g^{-1}	54.68 ± 0.50	67.4 ± 0.80	79.51 ± 0.50
$q_{m\ (theo)}$/mg·g^{-1}	65.95 ± 0.67	79.90 ± 1.28	100.46 ± 3.88
K_L/L·mg^{-1}	0.051 ± 0.001	0.069 ± 0.004	0.058 ± 0.004
R_L	0.40	0.33	0.37
R^2	0.999	0.997	0.995
SSE	6.84	40.28	186.34
χ^2	0.977	5.755	26.620
Freundlich			
K_F	7.50 ± 12.20	11.75 ± 1.80	12.18 ± 2.10
$1/n$	0.451 ± 0.026	0.434 ± 0.042	0.480 ± 0.059
R^2	0.957	0.965	0.915
SSE	352.6	533.6	3297.4
χ^2	50.4	76.2	471.1
Koble–Corrigan			
A	3.42 ± 0.20	4.93 ± 0.78	4.59 ± 0.57
B	0.051 ± 0.002	0.0642 ± 0.008	0.050 ± 0.005
n	0.987 ± 0.032	1.064 ± 0.086	1.119 ± 0.060
R^2	0.999	0.997	0.997
SSE	6.65	36.77	107.07
χ^2	1.11	6.13	17.84

$\Delta S°$ in Table 4 indicate no obvious change in entropy occurred during the adsorption process. The positive values $\Delta S°$ suggest an increase in randomness at the solid-solution interface that occurs on the surface of the adsorbent upon the adsorption of the dye and the nutrient [24]. The negative values of Gibbs free energy ($\Delta G°$) as presented in Table 4 indicate that the adsorption process of TNR@PEI–Zr towards AR and PO_4^{3-} is viable and thermodynamically spontaneous. The absolute value of ($\Delta G°$) increased as temperature increased, demonstrating that high temperatures were beneficial to the adsorption system. The positive activation energy (E_a) also relates to the favourability of increasing temperatures to the adsorption system. The observed E_a of 15.4 for AR and 29.5 for PO_4^{3-} kJ·mol^{-1} also suggests physisorption as described by Zhang *et al.* [45].

3.4. The adsorptive performance of TNR@PEI–Zr in real water samples

To evaluate the adsorptive performance of the engineered adsorbent for its practical use in a real environmental matrix, water samples from a man-made lake at Zhengzhou University together with tap water were used. About 10 mg of TNR@PEI–Zr was placed into 10 ml of each of the samples from the lake and tap water spiked with 5, 10 and 20 mg·L^{-1} of both AR and PO_4^{3-}. The mixtures were agitated

Table 4
Parameters of Thermodynamic studies for AR and PO_4^{3-} adsorption

Pollutant	$\Delta H°$/kJ·mol^{-1}	$\Delta S°$/kJ·mol^{-1}·K^{-1}	$\Delta G°$/kJ·mol^{-1}			E_a/kJ·mol^{-1}
			293 K	303 K	313 K	
AR	62.2	0.228	−4.47	−6.75	−9.02	15.4
PO_4^{3-}	25.3	0.090	−1.45	−2.36	−3.27	29.5

Table 5
Recovery of AR and PO_4^{3-} from real water samples

Pollutant	Environmental matrix	Spiked amount/mg·L^{-1}	Detected/mg·L^{-1}	Recovery/%	
				pH 3	upH①
Alizarin red	Lake	0	0.12	100.0 ± 0.4	100.0 ± 1.2
		5	5.24	99.7 ± 0.8	90.4 ± 2.0
		10	10.04	97.9 ± 3.3	90.0 ± 0.6
		20	20.30	98.5 ± 2.0	88.7 ± 4.2
	Tap	0	0.01	100.0 ± 1.0	91.8 ± 3.6
		5	4.90	99.8 ± 0.5	87.6 ± 1.1
		10	9.70	98.4 ± 2.0	86.4 ± 2.5
		20	19.80	98.0 ± 1.8	88.0 ± 3.6
Phosphate	Lake	0	0.00	0.00 ± 0.0	0.0 ± 0.0
		5	4.20	86.2 ± 1.1	75.6 ± 5.2
		10	8.70	83.6 ± 1.8	72.1 ± 4.6
		20	17.9	82.4 ± 2.4	71.6 ± 2.3
	Tap	0	0.00	0.00 ± 0.0	0.00 ± 0.0
		5	4.90	98.6 ± 2.5	82.2 ± 4.0
		10	10.1	95.4 ± 1.0	81.1 ± 2.5
		20	19.9	95.1 ± 1.0	85.8 ± 1.4

① upH: unregulated pH.

in an orbital shaker at 313 K for 60 min at an adjusted pH of 3 and an unadjusted pH of the dissolved pollutant. According to the findings in Table 5, there was no evidence of AR in the samples of lake or tap water. However, the levels of PO_4^{3-} found in samples of lake and tap water were 0.12 and 0.01 mg·L^{-1}, respectively, which is below the permitted limit set by the World Health Organization [46] as well as the U.S. Environmental Protection Agency [47]. It is clear from the recovery (%) findings that the altered pH helped TNR@PEI–Zr to efficiently recover the contaminants. The recovery for AR at pH 3 varied from (100.0 ± 0.4)% to (97.9 ± 3.3)% for lake water and from (100.0 ± 1.0)% to (98.0 ± 1.8)% for samples of tap water. Conversely, the recovery of PO_4^{3-} was (98.6 ± 2.5)% to (95.1 ± 1.0)% for tap water and (86.2 ± 1.1)% to (82.4 ± 2.4)% for lake water. Phosphate recovery from lake water samples was, by comparison, the lowest. This finding may be related to the possibility that certain salts are present in the lake water. These findings showed that TNR@PEI–Zr has excellent potential for usage in real-world wastewater clean-up applications.

3.5. Regeneration and reusability studies

Due to concerns about secondary pollution, studying the recyclability and the regeneration potential of newly engineered adsorbents is critical in profiling their applicability. TNR@PEI–Zr was successfully desorbed with 0.1 mol·L^{-1} NaOH for four consecutive adsorption–desorption cycles, as shown in Fig. 7(a). After four cycles, TNR@PEI–Zr exhibited 50% and 69% desorption and regeneration efficiency towards AR and recorded 87% and 95% desorption and regeneration efficiency towards PO_4^{3-}. The desorption and regeneration efficiency values suggest that the NaOH can destroy the interactions between TNR@PEI–Zr and AR and PO_4^{3-}. However, the reduced efficiencies at the fourth cycle could be explained by the fact that not all the earlier adsorbed ions of AR and PO_4^{3-} were desorbed. These observations are indicative of an economically viable and reusable adsorbent with an eco-friendly design process, making it favourable for the removal of AR and PO_4^{3-}.

3.6. Leaching test for TNR@PEI–Zr

From the leaching test, it was observed that the TNR@PEI–Zr did not leach into the solution at the studied pH of 2, 4 and 10. The concentration of zirconium was not detected in the supernatant from the solution with the TNR@PEI–Zr dosing after the 24 h agitation time (limit of detection was 0.1 μg·L^{-1} Zr(IV)). This finding implies that the zirconium was successfully incorporated into the adsorbent's fabric during the engineering procedure, resulting in its stability over a wide pH range. Hence, the practical application of this facile engineered adsorbent from tiger nut residue can be safely used in the environmental matrix without any concerns of secondary environmental pollution.

3.7. Adsorption mechanism of AR and PO_4^{3-} onto TNR@PEI–Zr

The adsorption processes of AR and PO_4^{3-} by TNR@PEI–Zr may be predicted from the characterizations and observations reported above. The very strong dependency of AR and PO_4^{3-} adsorption on the TNR@PEI–Zr surface chemistry confirms the active role of a significantly high electrostatic interactions subsisting between the anionic AR and PO_4^{3-} and the positively charged adsorbent surface observed in acidic medium. Decreasing solution pH in the range of 2–6 surged positive charges on the surface of TNR@PEI–Zr, that impelled more of the AR and PO_4^{3-} (Fig. 7(b)). Besides, the removal of AR and PO_4^{3-} were largely associated on ionic strength, indicating that the pollutant adsorption occurs in the outer sphere. This explains why increasing the concentration of salt resulted in a decrease in the adsorption capacity of the adsorbents towards the adsorbates due to competitive effects for adsorption sites between the salt ions and those dye molecules and phosphate ions [48]. In addition, protonated amino groups of TNR@PEI–Zr could have contributed to enhanced adsorption under acidic conditions. The adsorption mechanisms of AR and PO_4^{3-} were dominated by mono-layer adsorption of uneven surfaces both with chemisorption and physical adsorption, as evident from the better fit of the PSO kinetics and Langmuir isotherm with the experimental data. The SEM analysis (Fig. 1) provides images of the honeycomb porous surface of TNR@PEI–Zr which could capture and trap the molecules of AR and PO_4^{3-} ions, increasing their adsorption efficiency. The complexation interaction was a key adsorption mechanism owing to Zr as a transition metal to facilitate the adsorption of AR and PO_4^{3-} containing hydroxy groups to form the complex between TNR@PEI–Zr, AR and PO_4^{3-}. Results of aqueous experiments suggested the critical role of Zr on AR and PO_4^{3-} adsorption by TNR@PEI–Zr. Furthermore, the other mechanisms such as the π–π stacking and hydrogen bonding, may have contributed to the adsorptive performance of TNR@PEI–Zr. XPS analysis indicates the presence of carbon (C), nitrogen (N), oxygen (O), and zirconium (Zr), were detected on the surface of TNR@PEI–Zr before the adsorption. After AR and PO_4^{3-} adsorption, sulphur (S), and phosphorus (P) appeared on the spectrum, which demonstrated that alizarin red and phosphate were successfully adsorbed onto the surface of TNR@PEI–Zr. The full XPS spectra given in Fig. 3(b) and (c), shows peaks of S 2p and P 2p at 167.7 eV and 133.1 eV indicating that the AR molecules and phosphate groups were adsorbed onto TNR@PEI–Zr. Furthermore, Fig. 3(b) and (c) demonstrates the fractional changes in the elemental composition of C 1s, N 1s, O 1s and Zr 3d after the adsorption of AR and PO_4^{3-}, indicative of their involvement during the adsorption

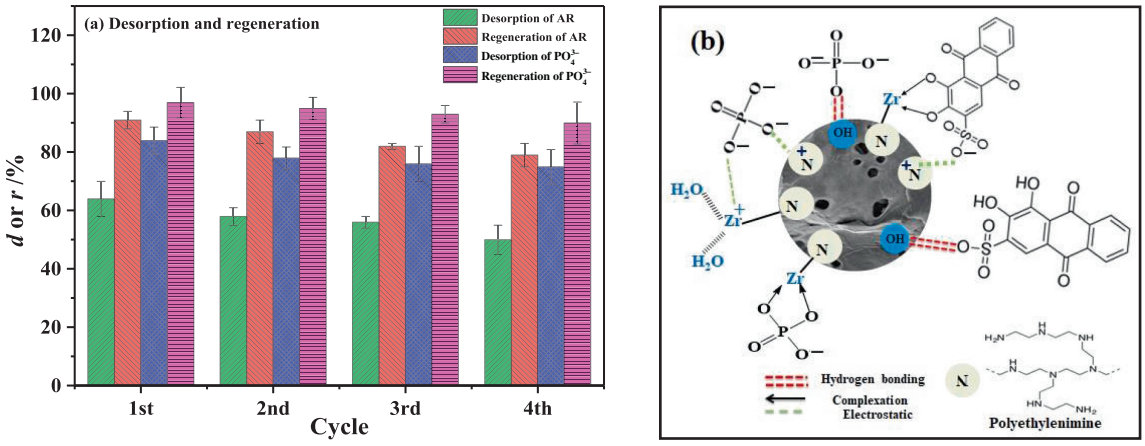

Fig. 7. Desorption and regeneration performance of TNR@PEI–Zr (a), and the possible adsorption mechanism of AR and PO_4^{3-} onto TNR@PEI–Zr (b).

Table 6a
Comparison of the adsorptive system of TNR@PEI–Zr towards Alizarin red with other recently reported adsorbents

Adsorbent	C_0/mg·L^{-1}	Dose/ g·L^{-1}	V/ ml	pH	t/ min	T/K	q_m/ mg·g^{-1}	Kinetic	Isotherm	Cycle	Enthalpy	Mechanism	Ref.
Fe_3O_4@NiO core–shell magnetic nanoparticles	100	1.5	50	7	60	288	223.3	PSO	Freundlich	6	Exothermic	Complexation, hydrogen bonding, π–π stacking	[49]
Amino-functionalized graphene oxide	100	0.015	10	2	60	301	135.1	IPD	Langmuir	N.A.	Endothermic	Electrostatic interactions	[50]
Cobalt hydroxide nanoparticles	351	0.043	10	5.5	40	RT	132.4	N.A.	Sips model	N.A.	Endothermic	N.A.	[51]
Zirconium and amine-grafted walnut shell biocomposite	200	0.01	10	3	420	303	415.5	PSO	Langmuir	3	Endothermic	Electrostatic interaction, complexation	[24]
Phenyl/amine end-capped tetraaniline	N.A.	2	20	N.A.	20	N. A.	236	N.A.	Langmuir	N.A.	Endothermic	Electrostatic interaction, π–π stacking	[52]
Sulphate cross-linked chitosan–bentonite composite	N.A.	0.2	50	8	40	303	131.58	PSO	Freundlich	N.A.	Exothermic	Electrostatic interaction, hydrogen bonding	[53]
Magnetic chitosan core–shell network	10	0.025	50	6.8	60	RT	166.4	PSO	Langmuir	5	N.A.	Electrostatic interaction	[54]
Iron (III) hydroxide doped chitosan sodium dodecyl sulfate (Chiron-SDS hydrogel bead)	50	2	5	5	3 h	353	294.12	PSO	Langmuir	N.A.	Endothermic	Electrostatic interaction, complexation, hydrogen bonding	[55]
Iron-based Fe–BTC MOF	1.5 mmo· L^{-1}	0.1	1	4	30	298	80	PSO	Langmuir	N.A.	N.A.	N.A.	[56]
Carbon composite-derived polymer phenolic resin	200	N.A.	N. A.	3	1440	298	104	PSO	Freundlich	N.A.	N.A.	N.A.	[57]
Diethylenetriamine and zirconium modified wheat straw	N.A.	N.A.	N. A.	6.4	N.A.	N. A.	164	PSO, Elovich	N.A.	N.A.	N.A.	N.A.	[58]
Fe_3O_4, iminodiacetic acid and zirconium modified peanut husk	100	1	10	5.7	120	313	49.4	PSO	Langmuir	3	Endothermic	Electrostatic interaction, complexation	[14]
Zr(IV)-loaded chitosan/Fe_3O_4/graphene oxide	200	1 g	10	5.7	360	313	231	PSO	Freundlich	N.A.	Endothermic	Electrostatic interaction, complexation, π–π stacking, hydrogen bonding, van der Waals forces	[12]
Calcium phosphate hydroxyapatite	150	0.1	100	7–8	60	303	100.36	PSO	Sips	N.A.	Endothermic	Electrostatic interaction	[41]
Hydrocellulose catechol-amine resin composite	150	0.05	100	upH	240	303	284.09	PSO	Langmuir	3	Endothermic	Electrostatic interaction, hydrogen bonding, π–π stacking	[59]
Polyaniline modified oxide-multi-walled carbon nanotubes	100	0.005	20	8.5	50	298	884.8	PSO	Langmuir	N.A.	Exothermic	N.A.	[60]
Spirulina platensis biomass	100	1.5	50	6.5	42.5	N. A.	17.15	PFO	Langmuir	4	N.A.	Electrostatic interaction	[61]
Calcined waste of eggshells	40	0.15	50	N.A.	120	298	156.56	PSO	Langmuir	5	Exothermic	N.A.	[42]
Silica grafted 3-aminopropyltriethoxysilane modified Micron-sized vermiculite clay	N.A.	0.8	25	2	20	283	59.8	PSO	Langmuir	N.A.	Endothermic	Electrostatic interaction, complexation	[62]
$NiFe_2O_4$/polyaniline magnetic composite	30	0.03	100	4.0–8.6	90	303	186	PSO	Langmuir	6	Endothermic	Electrostatic attraction, π–π stacking	[63]
Zirconium and polyaziridine based tiger nut residue	200	0.01	10	3	50	313	537.8	PSO	Langmuir	4	Endothermic	Electrostatic interaction, complexation, hydrogen bonding, π–π stacking	This study

Note: N.A. – not reported; upH – unadjusted pH; PFO – pseudo-first-order; PSO – pseudo-second-order; IDP – interparticle diffusion; T – temperature; t_e – equilibrium time.

Table 6b
Comparison of the adsorptive system of TNR@PEI–Zr towards phosphate with other recently reported adsorbents

Adsorbent	C_0/ mg·L^{-1}	Dose/ g·L^{-1}	V/ ml	pH	t_e/ min	T/K	q_m/ mg·g^{-1}	Kinetic	Isotherm	Cycle	Enthalpy	Mechanism	Ref.
Biochar–magnetite	8	6	20	2	180	N. A.	9.408	PSO	Langmuir and Freundlich	4	N.A.	Electrostatic interaction, ligand exchange	[64]
Biochar–ferrihydrite					120		18.49		Langmuir				
Biochar–goethite					60		22.14		Langmuir				
Biochar–hematite					120		13.81		Langmuir and Freundlich				
Powdered-acid–activated-neutralized red mud	500	3	N. A.	6	720	313	153.227	RN	Langmuir–Freundlich	N.A.	N.A.	Chemical precipitation, ion exchange, surface deposition	[65]
Zirconium ion modified MgAl-layered double hydroxides	0.92	15	50	7	360	298	54.3	PSO	Langmuir	N.A.	Endothermic	Complexation	[66]
Zirconium chloride octahydrate/CTAB/vetiver grass–activated carbon	15	0.3	50	3	120	308	4.2747	PSO	Freundlich	N.A.	Endothermic	Electrostatic, ion exchange	[67]
Polyethyleneimine-modified Bamboo biochar	20	20	N. A.	3	200	N. A.	9.258	PSO	Langmuir	N.A.	N.A.	Electrostatic interaction	[48]
Magnetic nanocomposite	300	0.5	N. A.	7	82	340	97	PSO	Freundlich	N.A.	Exothermic	Chemisorption	[40]
Amine functionalized walnut shells	30	1	10	5	60	293	82.2	PSO	Freundlich	N.A.	Exothermic	Electrostatic interaction, hydrogen bonding	[7]
Zirconium modified montmorillonite clay	30.66	1		7	N.A.	295	15.5	PSO	Langmuir	N.A.	N.A.	Complexation	[11]
Zirconium/aluminum-pillared montmorillonite	122.64	0.2	100	5	360	273	52.7	PSO	Langmuir	3	Endothermic	Electrostatic interaction	[68]
Magnetic zirconium-iron oxide nanoparticle	50	2	100	4	1000	293	21.3	PSO	Freundlich	3	Endothermic	Complexation	[25]
KOH deacetylated calcite based chitosan	61.32	1	50	UpH	120	295	65.5	PSO	Langmuir	N.A.	Endothermic	N.A.	[43]
Lanthanum-ammonia-modified hydrothermal biochar	N.A.	N.A.	N. A.	N.A.	N.A.	N. A.	132.1	PSO	Langmuir	N.A.	N.A.	Complexation	[69]
Lanthanum-iron incorporated chitosan beads	20	0.5	100	6.5	1440	298	159.432	PSO	Langmuir	4	N.A.	Electrostatic interaction, complexation, ligand exchange	[70]
Ferric oxyhydroxide loaded anion exchanger resin	50	0.025	100	2	390	313	85.46	PFO	Freundlich	N.A.	Endothermic	N.A.	[71]
Zeolite loaded with Mg–Al–La ternary (hydr)oxides (MOF)	306.6	0.2	50	6.6	180	298	247.7	PSO	Freundlich	4	N.A.	Complexation	[72]
Modified Rice straw	400	10	50	7	10	298	220.6	PSO	Langmuir	N.A.	Exothermic	N.A.	[6]
MOF-derived magnetic Fe–Ce bimetal oxide	100	0.4	50	6	1440	298	357	PSO	Langmuir	N.A.	N.A.	Magnetism	[73]
Zirconium and polyaziridine based tiger nut residue	30	1	10	3	60	313	100.5	PSO	Langmuir	4	Endothermic	Electrostatic attraction, complexation	This study

Note: N.A. – not reported; upH – unadjusted pH; PFO – pseudo-first-order; PSO – pseudo-second-order; IDP – interparticle diffusion; RN – Ritchie nth-order; T – temperature; t_e – equilibrium time.

process. The peaks of the deconvoluted O 1s of TNR@PEI–Zr after the adsorption process show the shift in the binding energies, indicating the likelihood of chemical interactions taking place in the adsorption process. Also, the peak around 532 and 533 eV corresponding to Zr—OH was observed, suggesting the occurrence of a complexation reaction between Zr and OH [14]. This is further confirmed by contrasting the deconvoluted peaks of TNR@PEI–Zr with that after adsorption, all the previous peaks report diminished peak intensities and a slight shift in their binding energies. The peak areas of the C—C groups had a remarkable decrease, while those of the C—O groups recorded a noticeable increased trend. These findings further demonstrate surface complexation involving oxygen-containing groups during the adsorption system.

3.8. Comparison of TNR@PEI–Zr with other adsorbents

Several adsorbents, including activated carbons, clay, chitosan, agricultural waste materials, metal organic framework (MOF), magnetic nanocomposite and their modified forms, have been employed in the adsorptive decontamination of both AR (Table 6a) and PO_4^{3-} (Table 6b). However, none of them have employed engineered tiger nut residue as used in this work. Alizarin Red and phosphate adsorption has been achieved within a wide pH range (2–8). However, most of the reported adsorptions occurred in the acidic medium. This suggests the adsorption of these pollutants is most efficient in acidic rather than alkaline medium and the behaviour of TNR@PEI–Zr was no different as it exhibited high adsorptive capability towards both AR and PO_4^{3-} in acidic medium. This behaviour of AR and phosphate explains why, in most cases, electrostatic interaction is posited as the main adsorption mechanism underpinning their removal. However, chemisorption processes including complexation, ligand exchange and precipitation have also been reported as possible mechanisms underlying the effective removal of AR and phosphate from solution. These mechanisms are largely influenced by the surface chemistry of the adsorbents and the pH of the solution. The kinetic process of AR decontamination has mostly been described by PSO, as seen in the present work (Table 6a). However, other models such as IPD [50], Elovich [58], and PFO [61] have also been verified to best fit the adsorption kinetics. On the other hand, apart from Ye *et al.* [65], whose kinetics suited the Ritchie nth-order, almost all the other works on phosphate removal found the PSO model to best explain their kinetic systems (Table 6b). Langmuir model is seen to fit most of the AR and PO_4^{3-} adsorption isotherms, with a few researchers indicating other isotherm models such as Freundlich [49,53,57] and Sips [41,51] to perfectly fit their experimental data. This gives credence to the chemisorption process as reported to mediate the removal process. The enthalpy process of both AR and PO_4^{3-} adsorption has been described by both endothermic and exothermic processes. From Tables 6a and 6b, it is observed that temperatures below 300 K seem to favour the removal of AR and PO_4^{3-}, but the maximum removal of AR and PO_4^{3-} by the engineered adsorbent used in this work was recorded at 313 K. On the adsorptive capacity of recently reported adsorbents toward AR and PO_4^{3-}, TNR@PEI–Zr outperforms many of them and compares well with some of the best adsorbents as presented in Tables 6a and 6b.

4. Conclusions

In the present study, the mechanisms and reusability potentials of zirconium-polyaziridine-engineered tiger nut residue toward anionic pollutants have been examined. The environmentally friendly engineering process of a biodegradable and low-cost tiger nut residue improved the material's surface characteristics, contributing to its efficient adsorptive performance towards AR and PO_4^{3-}. The various characterizations helped to confirm the modifications as well as the adsorption mechanism, which included electrostatic attraction and complexation coupled with hydrogen bonding. The effect of some common salts on the adsorption potential in AR and PO_4^{3-} was in the following order: $HCO_3^- > SO_4^{2-} > Cl^-$. The AR and PO_4^{3-} adsorption data fit the PSO kinetic model and the Langmuir isotherm model, implying chemisorption with homogenous and monolayer removal of pollutants at a maximum capacity of 537.8 $mg \cdot g^{-1}$ for AR and 100.5 $mg \cdot g^{-1}$ for PO_4^{3-}. Adsorption of AR and PO_4^{3-} by TNR@PEI–Zr is viable and thermodynamically spontaneous, with increased randomness at the solid-solution interface. TNR@PEI–Zr exhibited good reusability potential and outperformed several adsorbents in terms of its adsorption capacity. Studies with real water samples and the leaching test showed the adsorptive capability of TNR@PEI–Zr was stable, and as such, its practical usage in wastewater decontamination will not cause environmental concerns or secondary pollution.

Data Availability

Data will be made available on request.

Declaration of Competing Interest

The authors declare that they have no known competing financial interests or personal relationships that could have appeared to influence the work reported in this paper.

References

[1] N.V. Roik, L.A. Belyakova, M.O. Dziazko, Solubilization of azo dyes by cetyltrimethylammonium bromide micelles as structure control factor at synthesis of ordered mesoporous silicas, *J. Mol. Liq.* 328 (2021) 115451.
[2] A.N. Kani, E. Dovi, F.M. Mpatani, A.A. Aryee, R.P. Han, Z.H. Li, L.B. Qu, Pollutant decontamination by polyethyleneimine-engineered agricultural waste materials: A review, *Environ. Chem. Lett.* 20 (1) (2022) 705–729.
[3] Q.Z. Shao, Y. Li, Q. Wang, T. Niu, S. Li, W. Shen, Preparation of copper doped walnut shell-based biochar for efficiently removal of organic dyes from aqueous solutions, *J. Mol. Liq.* 336 (2021) 116314.
[4] S.K. Kansal, R. Lamba, S.K. Mehta, A. Umar, Photocatalytic degradation of Alizarin red S using simply synthesized ZnO nanoparticles, *Mater. Lett.* 106 (2013) 385–389.
[5] P.C. Bhomick, A. Supong, M. Baruah, C. Pongener, D. Sinha, Pine Cone biomass as an efficient precursor for the synthesis of activated biocarbon for adsorption of anionic dye from aqueous solution: Isotherm, kinetic, thermodynamic and regeneration studies, *Sustain. Chem. Pharm.* 10 (2018) 41–49.
[6] X.L. Huang, X. Sheng, Y. Guo, Y. Sun, P. Fatehi, H. Shi, Rice straw derived adsorbent for fast and efficient phosphate elimination from aqueous solution, *Ind. Crops Prod.* 184 (2022) 115105.
[7] E. Dovi, A.A. Aryee, J. Li, Z. Li, L. Qu, R. Han, Amine-grafted walnut shell for efficient removal of phosphate and nitrate, *Environ. Sci. Pollut. Res.* 29 (14) (2022) 20976–20995.
[8] A.N. Kani, E. Dovi, F.M. Mpatani, Z.H. Li, R.P. Han, L.B. Qu, Tiger nut residue as a renewable adsorbent for methylene blue removal from solution: Adsorption kinetics, isotherm, and thermodynamic studies, *Desalin. Water Treat.* 191 (2020) 426–437.
[9] J.H. Wang, X.H. Tong, S. Wang, Zirconium-modified activated sludge as a low-cost adsorbent for phosphate removal in aqueous solution, *Water Air Soil Pollut.* 229 (2) (2018) 1–10.
[10] W.P. Xiong, J. Tong, Z. Yang, G. Zeng, Y. Zhou, D. Wang, P. Song, R. Xu, C. Zhang, M. Cheng, Adsorption of phosphate from aqueous solution using iron–zirconium modified activated carbon nanofiber: Performance and mechanism, *J. Colloid Interface Sci.* 493 (2017) 17–23.
[11] J.W. Huo, X.P. Min, Y. Wang, Zirconium-modified natural clays for phosphate removal: Effect of clay minerals, *Environ. Res.* 194 (2021) 110685.
[12] M.Y. Liu, X. Zhang, Z. Li, L. Qu, R. Han, Fabrication of zirconium (IV)-loaded chitosan/Fe_3O_4/graphene oxide for efficient removal of alizarin red from aqueous solution, *Carbohydr. Polym.* 248 (2020) 116792.
[13] H. Cui, Q. Li, S. Gao, J.K. Shang, Strong adsorption of arsenic species by amorphous zirconium oxide nanoparticles, *J. Ind. Eng. Chem.* 18 (4) (2012) 1418–1427.
[14] A.A. Aryee, E. Dovi, Q.H. Guo, M.Y. Liu, R.P. Han, Z.H. Li, L.B. Qu, Selective removal of anionic dyes in single and binary system using zirconium and

iminodiacetic acid modified magnetic peanut husk, *Environ. Sci. Pollut. Res.* 28 (28) (2021) 37322–37337.
[15] A.N. Kani, E. Dovi, A.A. Aryee, F.M. Mpatani, R.P. Han, Z.H. Li, L.B. Qu, Polyethyleneimine modified tiger nut residue for removal of Congo red from solution, *Desalin. Water Treat.* 215 (2021) 209–221.
[16] Y.S. Ho, G. McKay, Pseudo-second order model for sorption processes, *Process Biochem.* 34 (5) (1999) 451–465.
[17] C. Aharoni, M. Ungarish, Kinetics of activated chemisorption. Part 1. The non-elovichian part of the isotherm, *J. Chem. Soc., Faraday Trans.* 1 (72) (1976) 400–408.
[18] W.J. Weber Jr, J.C. Morris, Kinetics of adsorption on carbon from solution, *J. Sanit. Engrg. Div.* 89 (2) (1963) 31–59.
[19] I. Langmuir, The adsorption of gases on plane surfaces of glass, mica and platinum, *J. Am. Chem. Soc.* 40 (9) (1918) 1361–1403.
[20] H.M.F. Freundlich, Over the adsorption in solution, *J. Phys. Chem.* 57 (1906) 385–471.
[21] R.A. Koble, T.E. Corrigan, Adsorption isotherms for pure hydrocarbons, *Ind. Eng. Chem.* 44 (2) (1952) 383–387.
[22] M.I. Temkin, V. Pyzhev, Kinetics of ammonia synthesis on promoted iron catalysts, *Acta Physiochim. URSS* 12 (1940) 217–222.
[23] A. El-Sayed, N. Awwad, M. Hamed, A.M.A. Hassan, S. El-Reefy, Simple and selective determination of Zr (IV) with 1,4-dichloro-2,5-dihydroxyquinone in a micellar solution of cetylpyridenium chloride by zero and second-derivative spectrophotometry, *Eur. J. Anal. Chem.* 12 (2) (2016) 151–165.
[24] E. Dovi, A.A. Aryee, M.Y. Liu, X.T. Zhang, A.N. Kani, J.J. Li, R.P. Han, L.B. Qu, Biocomposite based on zirconium and amine-grafted walnut shell with antibacterial properties for the removal of Alizarin red in water: Batch and column studies, *Environ. Sci. Pollut. Res.* 29 (60) (2022) 90530–90548.
[25] C. Zhang, Y. Li, F. Wang, Z. Yu, J. Wei, Z. Yang, C. Ma, Z. Li, Z. Xu, G. Zeng, Performance of magnetic zirconium–iron oxide nanoparticle in the removal of phosphate from aqueous solution, *Appl. Surf. Sci.* 396 (2017) 1783–1792.
[26] A.A. Aryee, E. Dovi, X. Shi, R. Han, Z. Li, L. Qu, Zirconium and iminodiacetic acid modified magnetic peanut husk as a novel adsorbent for the sequestration of phosphates from solution: Characterization, equilibrium and kinetic study, *Colloids Surf. A Physicochem. Eng. Aspects* 615 (2021) 126260.
[27] A.N. Kani, E. Dovi, A.A. Aryee, R.P. Han, L.B. Qu, Efficient removal of 2,4-D from solution using a novel antibacterial adsorbent based on tiger nut residues: Adsorption and antibacterial study, *Environ. Sci. Pollut. Res.* 29 (42) (2022) 64177–64191.
[28] T.T.Q. Nguyen, P. Loganathan, T.V. Nguyen, S. Vigneswaran, H.H. Ngo, Iron and zirconium modified luffa fibre as an effective bioadsorbent to remove arsenic from drinking water, *Chemosphere* 258 (2020) 127370.
[29] X.M. Dou, D. Mohan, C.U. Pittman, S. Yang, Remediating fluoride from water using hydrous zirconium oxide, *Chem. Eng. J.* 198–199 (2012) 236–245.
[30] M. Barathi, A.S. Kumar, N. Rajesh, A novel ultrasonication method in the preparation of zirconium impregnated cellulose for effective fluoride adsorption, *Ultrason. Sonochem.* 21 (3) (2014) 1090–1099.
[31] B.R. Poudel, R.L. Aryal, S.K. Gautam, K.N. Ghimire, H. Paudyal, M.R. Pokhrel, Effective remediation of arsenate from contaminated water by zirconium modified pomegranate peel as an anion exchanger, *J. Environ. Chem. Eng.* 9 (6) (2021) 106552.
[32] K.K. Zhu, Y.F. Gu, R. Wang, R.P. Han, Adsorption of catechol by Zr-loaded carbon nanotubes from solution, *Desalin. Water Treat.* 236 (2021) 274–284.
[33] A. Thøgersen, M. Syre, B. Retterstol Olaisen, S. Diplas, Studies of the oxidation states of phosphorus gettered silicon substrates using X-ray photoelectron spectroscopy and transmission electron microscopy, *J. Appl. Phys.* 113 (4) (2013) 044307.
[34] S.N. Basahel, M. Mokhtar, E.H. Alsharaeh, T.T. Ali, H.A. Mahmoud, K. Narasimharao, Photocatalytic degradation of *p*-nitrophenol in aqueous suspension by using graphene/ZrO_2 catalysts, *Nanosci. Nanotechnol. Lett.* 8 (5) (2016) 448–457.
[35] P.M. Shanthi, P.J. Hanumantha, K. Ramalinga, B. Gattu, M.K. Datta, P.N. Kumta, Sulfonic acid based complex framework materials (CFM): Nanostructured polysulfide immobilization systems for rechargeable lithium–sulfur battery, *J. Electrochem. Soc.* 166 (10) (2019) A1827–A1835.
[36] K.S. Siow, A. Rahman, A. Aminuddin, P.Y. Ng, Effect of sulfur on nitrogen-containing plasma polymers in promoting osteogenic differentiation of Wharton's Jelly mesenchymal stem cells, *Sains Malays* 50 (1) (2021) 239–251.
[37] A.M. Puziy, O.I. Poddubnaya, B. Gawdzik, J.M.D. Tascón, Phosphorus-containing carbons: Preparation, properties and utilization, *Carbon* 157 (2020) 796–846.
[38] J.W. Lin, Z. Zhang, Y.H. Zhan, Effect of humic acid preloading on phosphate adsorption onto zirconium-modified zeolite, *Environ. Sci. Pollut. Res.* 24 (13) (2017) 12195–12211.
[39] A.A. Shalaby, A.A. Mohamed, Determination of acid dissociation constants of Alizarin Red S, Methyl Orange, Bromothymol blue and Bromophenol blue using a digital camera, *RSC Adv.* 10 (19) (2020) 11311–11316.
[40] M. Fathy, M.A. Zayed, A.M.G. Mohamed, Phosphate adsorption from aqueous solutions using novel Zn Fe/Si MCM-41 magnetic nanocomposite: Characterization and adsorption studies, *Nanotechnol. Environ. Eng.* 4 (1) (2019) 1–12.
[41] A.I. Adeogun, R.B. Babu, One-step synthesized calcium phosphate-based material for the removal of Alizarin S dye from aqueous solutions: Isothermal, kinetics, and thermodynamics studies, *Appl. Nanosci.* 11 (7) (2021) 1–13.
[42] R. Slimani, H. Hiyane, M.E. Haddad, S. Lazar, S.E. Antri, Y. Achour, M. Essoufy, S. Benkaddour, I.E. Ouahabi, Removal efficiency of textile dyes from aqueous solutions using calcined waste of eggshells as eco-friendly adsorbent, *Chem. Biochem. Eng. Q.* 35 (1) (2021) 43–56.
[43] S. Pap, C. Kirk, B. Bremner, M. Turk Sekulic, L. Shearer, S.W. Gibb, M.A. Taggart, Low-cost chitosan-calcite adsorbent development for potential phosphate removal and recovery from wastewater effluent, *Water Res.* 173 (2020) 115573.
[44] H.N. Tran, E.C. Lima, R.S. Juang, J.C. Bollinger, H.P. Chao, Thermodynamic parameters of liquid-phase adsorption process calculated from different equilibrium constants related to adsorption isotherms: A comparison study, *J. Environ. Chem. Eng.* 9 (6) (2021) 106674.
[45] R.D. Zhang, J. Zhang, X. Zhang, C. Dou, R. Han, Adsorption of Congo red from aqueous solutions using cationic surfactant modified wheat straw in batch mode: Kinetic and equilibrium study, *J. Taiwan Inst. Chem. E.* 45 (5) (2014) 2578–2583.
[46] World Health Organization, Guidelines for drinking-water quality: Fourth edition incorporating the first addendum, (2017).
[47] U.S. Environmental Protection Agency, Quality criteria for water 1986: Office of Water, Washington, D.C., U.S. Environmental Protection Agency Report 440/5-86-001, 2019 (1986).
[48] T.T. Li, Z.H. Tong, B. Gao, Y.C. Li, A. Smyth, H.K. Bayabil, Polyethyleneimine-modified biochar for enhanced phosphate adsorption, *Environ. Sci. Pollut. Res.* 27 (7) (2020) 7420–7429.
[49] R. Nodehi, H. Shayesteh, A. Rahbar-Kelishami, Fe_3O_4@NiO core–shell magnetic nanoparticle for highly efficient removal of Alizarin red S anionic dye, *Int. J. Environ. Sci. Technol.* 19 (4) (2022) 2899–2912.
[50] W. Chananchana, P. Nuengmatcha, S. Chanthai, Role of cetyltrimethyl ammonium bromide on enhanced adsorption and removal of Alizarin red S using amino-functionalized graphene oxide, *Orient. J. Chem* 33 (6) (2017) 2920–2929.
[51] J. Zolgharnein, M. Bagtash, N. Asanjarani, Chemometrics approach for optimization of simultaneous adsorption of Alizarin red S and Congo red by cobalt hydroxide nanoparticles, *J. Chemom.* 31 (5) (2017) e2886.
[52] Y.P. Liu, J.J. Li, J.W. Zhu, W. Lyu, H. Xu, J.T. Feng, W. Yan, The adsorption property and mechanism of phenyl/amine end-capped tetraaniline for Alizarin red S, *Colloid Polym. Sci.* 296 (11) (2018) 1777–1786.
[53] M.A. Khapre, R.M. Jugade, Hierarchical approach towards adsorptive removal of Alizarin red S dye using native chitosan and its successively modified versions, *Water Sci. Technol.* 82 (4) (2020) 715–731.
[54] K. Rathinam, X. Kou, R. Hobby, S. Panglisch, Sustainable development of magnetic chitosan core–shell network for the removal of organic dyes from aqueous solutions, *Mater. Basel Switz.* 14 (24) (2021) 7701.
[55] N. Limchoowong, P. Sricharoen, S. Chanthai, A novel bead synthesis of the Chiron–sodium dodecyl sulfate hydrogel and its kinetics-thermodynamics study of superb adsorption of Alizarin red S from aqueous solution, *J. Polym. Res.* 26 (12) (2019) 1–11.
[56] G.R. Delpiano, D. Tocco, L. Medda, E. Magner, A. Salis, Adsorption of malachite green and Alizarin red S dyes using Fe–BTC metal organic framework as adsorbent, *Int. J. Mol. Sci.* 22 (2) (2021) 788.
[57] B. Wanassi, I.B. Hariz, C.M. Ghimbeu, C. Vaulot, M. Jeguirim, Green carbon composite-derived polymer resin and waste cotton fibers for the removal of Alizarin red S dye, *Energies* 10 (9) (2017) 1321.
[58] J.J. Zhang, J.H. Zhang, M.M. Yang, R.P. Han, Efficient sequestration of Alizarin red from solution using a novel adsorbent based on zirconium and diethylenetriamine functionalized wheat straw, *Desalin. Water Treat.* 235 (2021) 283–299.
[59] Q. Liu, Q.Z. Liu, Z.T. Wu, Y. Wu, T.T. Gao, J.S. Yao, Efficient removal of methyl orange and Alizarin red S from pH-unregulated aqueous solution by the catechol–amine resin composite using hydrocellulose as precursor, *ACS Sustain. Chem. Eng.* 5 (2) (2017) 1871–1880.
[60] K.Y. Wu, J.G. Yu, X.Y. Jiang, Multi-walled carbon nanotubes modified by polyaniline for the removal of Alizarin yellow R from aqueous solutions, *Adsorpt. Sci. Technol.* 36 (1–2) (2018) 198–214.
[61] E. Nasoudari, M. Ameri, M. Shams, V. Ghavami, Z. Bonyadi, The biosorption of Alizarin red S by *Spirulina platensis*; Process modelling, optimisation, kinetic and isotherm studies, *Int. J. Environ. Anal. Chem.* 103 (2023) 633–647.
[62] N. Ali, F. Ali, I. Ullah, Z. Ali, L. Duclaux, L. Reinert, J.M. Lévêque, A. Farooq, M. Bilal, I. Ahmad, Organically modified micron-sized vermiculite and silica for efficient removal of Alizarin red S dye pollutant from aqueous solution, *Environ. Technol. Innov.* 19 (2020) 101001.
[63] Y.D. Liang, Y. He, Y. Zhang, Q. Zhu, Adsorption property of Alizarin red S by $NiFe_2O_4$/polyaniline magnetic composite, *J. Environ. Chem. Eng.* 6 (1) (2018) 416–425.
[64] Z.R. Zhang, H.Q. Yu, R.X. Zhu, X. Zhang, L.G. Yan, Phosphate adsorption performance and mechanisms by nanoporous biochar–iron oxides from aqueous solutions, *Environ. Sci. Pollut. Res.* 27 (22) (2020) 28132–28145.
[65] J. Ye, X.N. Cong, P.Y. Zhang, E. Hoffmann, G.M. Zeng, Y. Wu, H.B. Zhang, W. Fan, Phosphate adsorption onto granular-acid-activated-neutralized red mud: Parameter optimization, kinetics, isotherms, and mechanism analysis, *Water Air Soil Pollut.* 226 (9) (2015) 1–10.
[66] H. Miyauchi, T. Yamamoto, R. Chitrakar, Y. Makita, Z.M. Wang, K.W. Jun, T. Hirotsu, Phosphate adsorption site on zirconium ion modified MgAl-layered double hydroxides, *Top. Catal.* 52 (6–7) (2009) 714–723.
[67] J.M. Li, X.Y. Fang, M. Yang, W. Tan, H.C. Zhang, Y.Y. Zhang, G.Z. Li, H.B. Wang, The adsorption properties of functionalization vetiver grass-based activated carbon: The simultaneous adsorption of phosphate and nitrate, *Environ. Sci. Pollut. Res.* 28 (30) (2021) 40544–40554.

[68] W.Y. Huang, J. Chen, F. He, J. Tang, D. Li, Y. Zhu, Y. Zhang, Effective phosphate adsorption by Zr/Al-pillared montmorillonite: Insight into equilibrium, kinetics and thermodynamics, *Appl. Clay Sci.* 104 (2015) 252–260.
[69] Z.X. Shang, Y. Wang, S. Wang, F. Jin, Z. Hu, Enhanced phosphorus removal of constructed wetland modified with novel lanthanum-ammonia-modified hydrothermal biochar: Performance and mechanism, *Chem. Eng. J.* 449 (2022) 137818.
[70] Z.C. Lan, Y. Lin, C. Yang, Lanthanum–iron incorporated chitosan beads for adsorption of phosphate and cadmium from aqueous solutions, *Chem. Eng. J.* 448 (2022) 137519.
[71] J. Ren, N. Li, L. Zhao, N.Q. Ren, Enhanced adsorption of phosphate by loading nanosized ferric oxyhydroxide on anion resin, *Front. Environ. Sci. Eng.* 8 (4) (2014) 531–538.
[72] W.M. Shi, Y. Fu, W. Jiang, Y. Ye, J. Kang, D. Liu, Y. Ren, D. Li, C. Luo, Z. Xu, Enhanced phosphate removal by zeolite loaded with Mg–Al–La ternary (hydr) oxides from aqueous solutions: Performance and mechanism, *Chem. Eng. J.* 357 (2019) 33–44.
[73] S.X. Yang, Q. Wang, H. Zhao, D. Liu, Bottom-up synthesis of MOF-derived magnetic Fe–Ce bimetal oxide with ultrahigh phosphate adsorption performance, *Chem. Eng. J.* 448 (2022) 137627.